Asteroseismology for "à la carte" stellar age-dating and weighing Age and mass of the CoRoT exoplanet host HD 52265

Y. Lebreton^{1,2} and M.J. Goupil³

- Observatoire de Paris, GEPI, CNRS UMR 8111, F-92195 Meudon, France
- Institut de Physique de Rennes, Université de Rennes 1, CNRS UMR 6251, F-35042 Rennes, France e-mail: yveline.lebreton@obspm.fr
- ³ Observatoire de Paris, LESIA, CNRS UMR 8109, F-92195 Meudon, France

Received, 2012; accepted, 2012

ABSTRACT

Context. In the context of the space missions CoRoT, Kepler, Gaia, TESS, and PLATO, precise and accurate stellar ages, masses, and radii are of paramount importance. For instance, they are crucial for constraining scenarii of planetary formation and evolution.

Aims. We aim at quantifying how detailed stellar modelling can improve the accuracy and precision on age and mass of individual stars. To that end, we adopt a multifaceted approach where we carefully examine how the number of observational constraints as well as the uncertainties on observations and on model input physics affect the results of age-dating and weighing.

Methods. We modelled* in detail the exoplanet host-star HD 52265, a main-sequence, solar-like oscillator that CoRoT observed for four months. We considered different sets of observational constraints (Hertzsprung-Russell data, metallicity, various sets of seismic constraints). For each case, we determined the age, mass, and properties of HD 52265 inferred from stellar models, and we quantified the impact of the model input physics and free parameters. We also compared model ages with ages derived by empirical methods or Hertzsprung-Russell diagram inversion.

Results. For our case study HD 52265, our seismic analysis provides an age A = 2.10 - 2.54 Gyr, a mass M = 1.14 - 1.32 M_{\odot} , and a radius R = 1.30 - 1.34 R_{\odot} , which corresponds to age, mass, and radius uncertainties of ~ 10 , ~ 7 , and ~ 1.5 per cent, respectively. These uncertainties account for observational errors and current state-of-the-art stellar model uncertainties. Our seismic study also provides constraints on surface convection properties through the mixing-length, which we find to be 12 - 15 per cent lower than the solar value. On the other hand, because of helium-mass degeneracy, the initial helium abundance is determined modulo the mass value. Finally, we evaluate the seismic mass of the exoplanet to be $M_p \sin i = 1.17 - 1.26$ M_{Jupiter} , much more precise than what can be derived by Hertzsprung-Russell diagram inversion.

Conclusions. We demonstrate that asteroseismology allows us to substantially improve the age accuracy that can be achieved with other methods. We emphasize that the knowledge of the mean properties of stellar oscillations - such as the large frequency separation-is not enough to derive accurate ages. We need precise individual frequencies to narrow the age scatter that is a result of the model input physics uncertainties. Further progress is required to better constrain the physics at work in stars and the stars helium content. Our results emphasize the importance of precise classical stellar parameters and oscillation frequencies such as will be obtained by the Gaia and PLATO missions.

Key words. asteroseismology - stars: interiors - stars:evolution -stars:oscillations - stars: individual: HD 52265 -stars: fundamental parameters -planets and satellites: fundamental parameters

1. Introduction

Stellar ages are crucial input parameters in many astrophysical studies. For instance, the knowledge of the stellar formation rate and age-metallicity relation (Gilmore 1999; Hernandez et al. 2000) is essential for understanding the formation and evolution of our Galaxy (Freeman 1993). In addition, precise ages of the oldest Galactic halo stars are essential to set a lower limit to the age of the Universe (Watson 1998). Moreover, the huge harvest of newly discovered exoplanets calls for accurate and precise ages of their host stars, a crucial parameter for understanding planet formation and evolution (Havel et al. 2011).

While stellar masses and/or radii can be measured directly for some particular stars – masses and radii for members of binary systems, radii for giant stars or bright dwarfs observable

by interferometry - stellar ages cannot be determined by direct measurements, but can only be estimated or inferred. As reviewed by Soderblom (2010), there are many methods to estimate the age of a star according to its mass, evolutionary state, and configuration - single star or star in a group. The ages of single main-sequence (MS) stars are often inferred from empirical indicators (activity or rotation) and/or from stellar model isochrones that are compared with observed classical parameters such as effective temperature $T_{\rm eff}$, luminosity L or surface gravity $\log g$, and metallicity [Fe/H]. However, the precision and accuracy that can currently be reached are not good enough to precisely characterize exoplanets (Havel et al. 2011). Several error sources hamper single-star age-dating: errors on the observational data, internal error related to the age-dating method, and, for stellar-model-dependent methods, degree of realism of the models. Depending on the mass and evolutionary stage and on the method, the error on age may be in the range of 50 to more

^{*} Tables 4, 5, A.2, A.3, A.4, A.5 are also available in electronic form at the CDS via anonymous ftp to cdsarc.u-strasbg.fr (130.79.128.5) or via http://cdsweb.u-strasbg.fr/cgi-bin/qcat?J/A+A/

than 150 per cent (see for instance Lebreton & Montalbán 2009, and references therein).

Indeed, stellar model outputs, as the age attributed to a given star, are quite sensitive to the physical inputs of the model calculation. For instance, the processes of transporting or mixing chemical elements, such as convection and overshooting, microscopic diffusion, and turbulent diffusion induced by hydrodynamical instabilities have been found to have a major impact. Unfortunately, these processes are still only poorly described and often have to be parametrized.

Progress is made with the availability of asteroseismic data provided by the high-precision photometric missions CoRoT (Baglin et al. 2002) and Kepler (Koch et al. 2010). Lowamplitude solar-like oscillations have been detected in many stars, and their frequencies have been measured with a precision typically of a few tenths of micro Hertz (e.g. Michel et al. 2008; Chaplin & Miglio 2013). Seismic data have recently and very frequently been used to age-date and weigh stars. Currently, two approaches are taken. The first one, ensemble asteroseismology, attempts to determine the mass and age of large sets of stars based on their mean seismic properties (Chaplin et al. 2014). In this approach, interpolation in large grids of stellar models by different techniques provides the mass and age of the model that best matches the observations. The alternative approach, which is more precise, is the hereafter named "à la carte" modelling¹ (Lebreton 2013), that is, the detailed study of specific stars, one by one, also referred to as "boutique" modelling, (see e.g. D. Soderblom, 2013, invited review at the International Francqui Symposium²). This approach has been used to model CoRoT and Kepler stars (see the reviews by Baglin et al. 2013; Chaplin & Miglio 2013). Stars hosting exoplanets have been modelled for example by Gilliland et al. (2011), Lebreton (2012), Escobar et al. (2012), Lebreton (2013), and Gilliland et al. (2013).

In the present study, we address the specific problem of quantifying the sources of inaccuracy that affect the estimates of age, mass, and radius of stars. In the past, Brown et al. (1994) addressed this problem theoretically, while Lebreton et al. (1995) discussed it in an early prospective study related to the preparation of the Gaia-ESA mission. The need for this quantification has become even more crucial because age, mass and radius of exoplanet host-stars are key to characterizing the planets and then to understanding their formation and evolution. This is therefore a prerequisite in the context of the space missions CoRoT, Kepler, and forthcoming Gaia, TESS, and PLATO. Recently, Valle et al. (2014) used a grid approach and a synthetic sample of solar-type MS stars to carry out a theoretical investigation to identify and quantify the sources of biases on the mass and radius determinations. Here we instead consider the à la carte approach to characterize a main CoRoT target, HD 52265, as an illustrative case-study. The G-type metal-rich star HD 52265 is a MS star that hosts an exoplanet whose transit was not observable, but CoRoT provided a rich solar-like oscillation spectrum that was analysed by Ballot et al. (2011) and Gizon et al. (2013). HD 52265 has been modelled by Soriano et al. (2007) prior to its observation by CoRoT, and then by Escobar et al. (2012) and Lebreton & Goupil (2012) on the basis of CoRoT data. The asteroseismic modelling by Escobar et al. (2012) was based on the large and small mean frequency separations (see Sect. 2). It provided a seismic mass of

 $1.24 \pm 0.02~M_{\odot}$, a seismic radius of $1.33 \pm 0.02~R_{\odot}$, and a seismic age of 2.6 ± 0.2 Gyr. Note that the error bars on these values do not include the impact of the uncertainties on stellar model inputs. The mass of the exoplanet was not evaluated either.

In this study, we characterize the star in terms of age, mass, radius, initial helium content, etc. To that end, we performed à la carte modelling based on several classes of dedicated stellar models corresponding to different assumptions on the input physics and chemical composition, and we used different sets of observational parameters to constrain the models. We examined how the uncertainties on the observational constraints and on the model input physics and free parameters affect the results of stellar modelling.

In Sect. 2, we review the observational data available for HD 52265. In Sect. 3, we describe our methodology and choices for cases of interest. The results are detailed in Sect.4, namely the range of age, mass, radius, initial helium content, and mixing-length parameter of the models. They show that using seismic constraints severely restricts these ranges. For comparison, Sect. 5.1 discusses the empirical ages of the star, while Sect. 5.2 presents ages obtained through isochrone placement in the Hertzsprung-Russell (H-R) diagram. We discuss the impact of the uncertainty on the mass of the host-star on the mass of the exoplanet in Sect. 6, and we draw some conclusions in Sect. 7.

2. Observational constraints for HD 52265

This section reviews the observational data that we used as constraints for the modelling of HD 52265.

2.1. Astrometry, photometry, and spectroscopy

HD 52265 (HIP 33719) is a nearby single G0V star. According to its Hipparcos parallax $\pi=34.53\pm0.40$ mas (van Leeuwen 2007), it is located at \approx 29 pc. To model the star, we considered the observational data listed in Table 1. In the literature, we gathered twenty spectroscopic determinations of the effective temperature T_{eff} , surface gravity $\log g$, and metallicity [Fe/H] of HD 52265 reported since 2001. We adopted here the average of these quantities and derived the error bars from the extreme values reported. To derive the luminosity L, we used the parallax and the Tycho V_T magnitude, V_T =6.358±0.004 mag, which we translated into the Johnson value, $V_{\rm J} = 6.292 \pm 0.005$ mag, following Mamajek et al. (2002). The bolometric correction BC= -0.014 ± 0.012 was derived from $T_{\rm eff}$, log g, and [Fe/H] using the tools developed by VandenBerg & Clem (2003). The Stefan-Boltzmann radius corresponding to the adopted values of L and $T_{\rm eff}$ is $R_{\rm SB} = 1.28 \pm 0.06 R_{\odot}$.

Butler et al. (2000) detected an exoplanet through observed radial velocity (RV) variations of HD 52265. From the RV curve they derived the semi-amplitude K, orbital period P, eccentricity e, and semi-major axis a of the orbit. From RV data and the Kepler third law, a lower limit on the mass of the planet can be inferred, via

$$M_{\rm p}\sin i = M_{\rm star}^{2/3}K(1 - e^2)^{1/2}(P/2\pi G)^{1/3},\tag{1}$$

where i is the angle of inclination of the orbital plane on the sky (see e.g. Perryman 2011). This is discussed in more detail in Sect. 6.

¹ We use "à la carte" in opposition to "set meal" to stress the point that models are specifically fashioned to study a case-study star.

http://fys.kuleuven.be/ster/meetings/francqui

Table 1. Main observational constraints for the modelling of HD 52265.

$T_{ m eff}$	$\log g$	[Fe/H]	L	$\langle \Delta \nu \rangle$	$\Delta v_{ m asym}$	$\langle d_{02} \rangle$	$\langle r_{02} \rangle$	$\langle rr_{01/10}\rangle$
[K]	[dex]	[dex]	$[L_{\odot}]$	$[\mu Hz]$	$[\mu Hz]$	$[\mu \text{Hz}]$	_	_
6116 ± 110	4.32 ± 0.20	0.22 ± 0.05	2.053 ± 0.053	98.13 ± 0.14	98.19 ± 0.05	8.20 ± 0.31	0.084 ± 0.003	0.033 ± 0.002

2.2. CoRoT light-curve inferences and seismic constraints

Ultra high-precision photometry of HD 52265, performed onboard CoRoT for four months, provided a light-curve carrying the solar-like oscillation signature (Ballot et al. 2011).

2.2.1. Individual oscillation frequencies

HD 52265 shows a pressure-mode (p-mode) solar-like oscillation spectrum, in which Ballot et al. (2011) identified 28 reliable low-degree p-modes of angular degrees $\ell=0,1,2$ and radial orders n in the range 14-24 (see their Table 4). The frequencies $\nu_{n,\ell}$ are in the range 1500-2550 μ Hz. Because the data are of high quality, the precision on each frequency is of a few tenths of μ Hz.

In the present study, individual frequencies were used to constrain stellar models. Before turning to the problems related to the use of individual frequencies, we briefly recall some basic properties of stellar oscillations.

A formulation adapted from the asymptotic expansion by Tassoul (1980) is commonly used to interpret the observed low-degree oscillation spectra (see e.g. Mosser et al. 2013, and references therein). It approximates the frequency of a p-mode of high radial order n and angular degree $\ell \ll n$ as

$$v_{n,\ell} \simeq \left(n + \frac{1}{2}\ell + \epsilon\right) \Delta v_{\text{asym}} - \ell(\ell+1)D_0,$$
 (2)

where the coefficients ϵ , $\Delta v_{\rm asym}$, and D_0 depend on the considered equilibrium state of the star. In particular

$$\Delta \nu_{\text{asym}} = \left(2 \int_{0}^{R} \frac{dr}{c}\right)^{-1} \text{ and } D_0 \approx -\frac{\Delta \nu_{\text{asym}}}{4\pi^2 \nu_{n,\ell}} \int_{0}^{R} \frac{dc}{r},$$
 (3)

where c is the adiabatic sound speed $c = (\Gamma_1 P/\rho)^{1/2}$ (Γ_1 is the first adiabatic index, P the pressure, and ρ the density). For a perfect gas, $c \propto (T/\mu)^{\frac{1}{2}}$ where T is the temperature and μ the mean molecular weight.

The quantity $\Delta \nu_{\rm asym}$ measures the inverse of the sound travel time across a stellar diameter and is proportional to the square root of the mean density, while D_0 probes the evolution status (and then age) through the sound speed gradient built by the chemical composition changes in the stellar core.

The ϵ term weakly depends on n and ℓ but is highly sensitive to the physics of surface layers. The problem is that outer layers in solar-type oscillators are the seat of inefficient convection, a 3-D turbulent process, which is poorly understood. The modelling of near-surface stellar layers is uncertain and so are the related computed frequencies. These so-called near-surface effects are a main concern when using individual frequencies to constrain stellar models because they are at the origin of an offset between observed and computed oscillation frequencies. Some empirical recipes can be used to correct for this offset. This is discussed in more detail in Sect. 3.2.

2.2.2. $\nu_{\rm max}$, $\langle \Delta \nu \rangle$, and scaling relations

From the oscillation power spectrum of HD 52265, Ballot et al. (2011) extracted the frequency at maximum amplitude $\nu_{\rm max} = 2090 \pm 20~\mu{\rm Hz}$. This quantity is proportional to the acoustic cutoff frequency, itself related to effective temperature and surface gravity (see e.g. Brown et al. 1994; Kjeldsen & Bedding 1995; Belkacem et al. 2011). This yields a scaling relation that can be used to constrain the mass and radius of a star of known $T_{\rm eff}$,

$$\nu_{\text{max,sc}}/\nu_{\text{max,}\odot} = (M/M_{\odot})(T_{\text{eff}}/5777)^{-1/2}(R/R_{\odot})^{-2},$$
 (4)

where $\nu_{\text{max},\odot} = 3050 \ \mu\text{Hz}$ is the solar value and the index sc stands for scaling.

The difference in frequency of two modes of same degree and orders that differ by one unit reads

$$\Delta \nu_{\ell}(n) = \nu_{n,\ell} - \nu_{n-1,\ell},\tag{5}$$

and is named the large frequency separation. We used the mean large frequency separation to constrain stellar models and calculated it in three different ways, but each time the observational value and the model value were calculated accordingly.

First, the mean large frequency separation can be calculated as an average of the individual separations defined by Eq. 5. We first calculated the mean separation $\langle \Delta \nu_\ell \rangle$ for each observed angular degree ($\ell=0,1,2$) by averaging over the whole range of observed radial orders. We then obtained the overall mean sepa-

ration from
$$\langle \Delta \nu \rangle = \frac{1}{3} \sum_{\ell=0}^{2} \langle \Delta \nu_{\ell} \rangle$$
. Its value is reported in Table 1.

Second, in the asymptotic approximation (Eq. 2), $\Delta \nu_\ell(n) \equiv \Delta \nu_{\rm asym}$ is approximately constant regardless of the ℓ value. We carried out a weighted least-squares fit of the asymptotic relation, Eq. 2, to the 28 identified frequencies and obtained the value of $\Delta \nu_{\rm asym}$ given in Table 2, as well as D_0 (1.43 \pm 0.05 μ Hz) and ϵ (1.34 \pm 0.01). The quoted error bars were inferred from a Monte Carlo simulation.

Third, as mentioned in Sect. 2.2.1, $\langle \Delta \nu \rangle \propto \langle \rho \rangle^{1/2}$. This yields a scaling relation that can be used to constrain stellar mass and radius (see e.g. Ulrich 1986; Kjeldsen & Bedding 1995),

$$\langle \Delta \nu \rangle_{\rm sc} / \langle \Delta \nu \rangle_{\odot} = (M/M_{\odot})^{1/2} (R/R_{\odot})^{-3/2}, \tag{6}$$

where $\langle \Delta \nu \rangle_{\odot} = 134.9 \,\mu\text{Hz}.$

The inversion of Eqs. 4 and 6, with the observed values of $\langle \Delta \nu \rangle$, $\nu_{\rm max}$, and $T_{\rm eff}$ of Table 1, yields $R_{\rm sc} = 1.33 \pm 0.02~R_{\odot}$, $M_{\rm sc} = 1.25 \pm 0.05~M_{\odot}$, and $\log~g_{\rm sc} = 4.29 \pm 0.01$ dex.

2.2.3. Small frequency separations and separation ratios

The difference in frequency of two modes of degrees that differ by two units and orders that differ by one unit reads

$$d_{\ell, \ell+2}(n) = \nu_{n,\ell} - \nu_{n-1, \ell+2} \tag{7}$$

and is commonly referred to as the small frequency separation.

Modes of $\ell=1$ are rather easy to detect, while modes of $\ell=2$ are not always observed or are affected by large error bars. This led Roxburgh & Vorontsov (2003) to propose to use the five

points small separations $dd_{01}(n)$ and $dd_{10}(n)$ as diagnostics for stellar models. They read

$$dd_{01}(n) = \frac{1}{8}(\nu_{n-1,0} - 4\nu_{n-1,1} + 6\nu_{n,0} - 4\nu_{n,1} + \nu_{n+1,0})$$
 (8)

$$dd_{10}(n) = -\frac{1}{8}(\nu_{n-1,1} - 4\nu_{n,0} + 6\nu_{n,l} - 4\nu_{n+1,0} + \nu_{n+1,1}). \tag{9}$$

According to the asymptotic relation (Eq. 2), $d_{02}(n)$ scales as $\approx 6D_0$, while $dd_{01/10}(n)$ scales as $\approx 2D_0$. Thus, they all probe the evolutionary status of stars.

Furthermore, Roxburgh & Vorontsov (2003) demonstrated that while the frequency separations are sensitive to near-surface effects, these effects nearly cancel in the frequency separation ratios defined as

$$r_{02}(n) = d_{02}(n)/\Delta v_1(n)$$
 (10)

$$rr_{01}(n) = dd_{01}(n)/\Delta v_1(n)$$
; $rr_{10}(n) = dd_{10}(n)/\Delta v_0(n+1)$. (11)

As detailed in the following, we used these frequency separations and ratios to constrain models of HD 52265. We denote by $\langle d_{02} \rangle$, $\langle r_{02} \rangle$ and $\langle rr_{01/10} \rangle$, the mean values of the small frequency separations and separation ratios. To calculate the mean values given in Table 2, we averaged over the whole range of observed radial orders.

2.2.4. Related seismic diagnostics

Ulrich (1986) and Christensen-Dalsgaard (1988) proposed to use the pair $(\langle \Delta \nu \rangle)$ and $\langle d_{02} \rangle$ as a diagnostic of age and mass of MS stars. To minimize near-surface physics the $(\langle \Delta \nu \rangle)$ and $\langle r_{02} \rangle$ pair can be used instead (Otí Floranes et al. 2005).

The advantage of $\langle r_{02} \rangle$ is that it decreases regularly as evolution proceeds on the MS. But when only modes of $\ell=1$ are observed, it is interesting to consider the mean ratios $\langle rr_{01/10} \rangle$, which are also sensitive to age (see e.g. Miglio & Montalbán 2005; Mazumdar 2005). This is illustrated in Fig. 1, which shows the run of $(\langle rr_{01} \rangle + \langle rr_{10} \rangle)/2$ as a function of $\langle \Delta v \rangle$ along the evolution on the MS of stars of different masses. For all masses, the $\langle rr_{01/10} \rangle$ ratio decreases at the beginning of the evolution on the MS to a minimum and then increases to the end of the MS. The lowest value is higher and occurs earlier as the mass of the star increases, that is as a convective core appears and develops.

Deviations from the asymptotic theory are found in stars as soon as steep gradients of physical quantities build up. This occurs for instance at the boundaries of convective zones because of the abrupt change of energy transport regime. Such glitches affect the sound speed, and an oscillatory behaviour is then visible in frequency differences (see e.g. Gough 1990; Audard & Provost 1994; Roxburgh & Vorontsov 1994). In Lebreton & Goupil (2012), we used the oscillatory behaviour of the observed $rr_{01}(n)$ and $rr_{10}(n)$ ratios to estimate the amount of convective penetration below the convective envelope of HD 52265.

2.2.5. Rotation period and inclination of the rotation axis

Ballot et al. (2011) derived a precise rotation period, $P_{\rm rot} = 12.3\pm0.14$ days from the light curve. Gizon et al. (2013) used seismic constraints to estimate the inclination of the spin axis of HD 52265 and found $\sin i = 0.59^{+0.18}_{-0.14}$. This allows us to estimate the mass of the exoplanet detected by RV variations (Butler et al. 2000), under the standard assumption that the stellar rotation axis is the same as the axis of the exoplanet orbit (see Sect. 6).

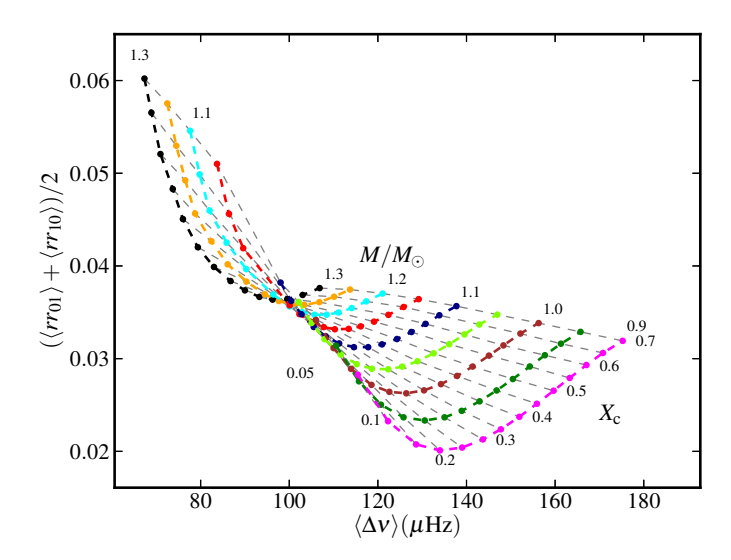


Fig. 1. Asteroseismic diagram showing the run of $(\langle rr_{01} \rangle + \langle rr_{10} \rangle)/2$ as a function of $\langle \Delta \nu \rangle$ for stars with masses in the range $0.9-1.3~M_{\odot}$ during the MS. Models have been calculated with an initial helium abundance Y=0.275, solar metallicity Z/X=0.0245, and mixing-length parameter $\alpha_{\rm conv}=0.60$. Evolutionary stages with decreasing central hydrogen abundance $X_{\rm c}$ are pinpointed.

3. Searching for an optimal model of HD 52265

We present the optimization method we used to obtain a model that best matches a selected set of observational constraints. We considered several choices of observational constraints, as explained in Sect. 3.4. First, we chose a reference set of input physics for the modelling and, for this set, the optimization gave us a reference model for each selected case of observational constraints. In a second step, we carried out additional optimizations based on other possible choices for the input physics. We then quantified the age and mass uncertainties, for instance by comparing the additional models to the reference one. Below we first present the inputs of the models (Sect. 3.1), then the calculation of the oscillation frequencies (Sect. 3.2), and finally the optimization method (Sect. 3.3) and the choice of the sets of observational constraints (Sect. 3.4).

3.1. Model input physics and chemical composition

We have modelled the star with the stellar evolution code Cesam2k (Morel & Lebreton 2008; Marques et al. 2013). Following Lebreton et al. (2008), to ensure numerical accuracy, the models were calculated with ≈ 2000 mesh points and ≈ 100 time steps were taken to reach the optimized final model of the star. Our aim has been to evaluate the effect of the choice of the model input physics on the inferred age, mass, and radius of HD 52265. We considered the input physics, and parameters described below and listed in Table 2.

– Opacities, equation of state (EoS), nuclear reaction rates: Our reference models (set A, Table 2) are based on the OPAL05 EoS (Rogers & Nayfonov 2002) and on OPAL96 opacities (Iglesias & Rogers 1996) complemented at low temperatures by WICHITA tables (Ferguson et al. 2005). We used the NACRE nuclear reaction rates (Angulo et al. 1999) except for the $^{14}N(p,\gamma)^{15}O$ reaction, where we adopted the revised

- LUNA rate (Formicola et al. 2004). To estimate uncertainties, we also calculated models based on the OPAL01 EoS (set H) and the NACRE nuclear reaction rate for the $^{14}N(p,\gamma)^{15}O$ reaction (set D).
- Microscopic diffusion: Our reference models take into account the microscopic diffusion of helium and heavy elements including gravitational settling, thermal and concentration diffusion but no radiative levitation, following the formalism of Michaud & Proffitt (1993, hereafter MP93). Note that Escobar et al. (2012) showed that radiative accelerations do not affect the structure of the models of HD 52265. To estimate uncertainties, we calculated models without diffusion (set E), and in set G models with diffusion, but treated with the Burgers formalism (Burgers 1969, hereafter B69). In a test, we investigated the effect of mixing that results from the radiative diffusivity associated with the kinematic radiative viscosity v_{rad} (subset A described in Appendix A). According to Morel & Thévenin (2002), it can be modelled by adding an additional mixing with a diffusion coefficient $d_{\rm rad} = D_{\rm R} \times v_{\rm rad}$ with $D_{\rm R} \approx 1$. It limits gravitational settling in the outer stellar layers of stars with thin convective envelopes.
- Convection: Our reference is the CGM convection theory of Canuto et al. (1996), which includes a free mixing-length parameter $\alpha_{\text{conv}} = \ell/H_P$ (ℓ is the mixing length and H_P the pressure scale height). To estimate uncertainties, we considered in set B the MLT theory (Böhm-Vitense 1958). When enough observational constraints were available, the value of α_{conv} was derived from the optimization of the models. When too few observational constraints were available, the value of the mixing length had to be fixed. For the reference model, it was fixed to the solar value $\alpha_{\text{conv,cgm}} = 0.688$ or $\alpha_{\text{conv,mlt}} = 1.762$, which results from the calibration of the radius and luminosity of a solar model with the same input physics (see e.g. Morel & Lebreton 2008). Other choices for the mixing length are considered in the study and presented in Appendix A.
- <u>Core overshooting</u>: In reference models we did not consider overshooting. We explored its impact in alternate models where we assumed that the temperature gradient in the overshooting zone is adiabatic. A first option (set I) was to set the core overshooting distance to be $\ell_{\rm ov,c} = \alpha_{\rm ov} \times \min(R_{\rm cc}, H_P)$, where $R_{\rm cc}$ is the radius of the convective core and $\alpha_{\rm ov} = 0.15$. In a second option (set J), we adopted the Roxburgh (1992) prescription, in which overshooting extends on a fraction of the mass of the convective core $M_{\rm cc}$, the mass of the mixed core being expressed as $M_{\rm ov,c} = \alpha_{\rm ov} \times M_{\rm cc}$ with $\alpha_{\rm ov} = 1.8$.
- Convective penetration: Convective penetration below the convective envelope is the penetration of fluid elements into the radiative zone due to their inertia. It leads to efficient convective heat transport with penetrative flows that establish a close to adiabatic temperature gradient, and to an efficient mixing of material in the extended region. A model for convective penetration has been designed by Zahn (1991). In this model, the distance of fluid penetration into the radiative zone reads $L_p = \frac{\xi_{\rm PC}}{\chi_p} H_P$, where $\chi_P = (\partial \log \chi / \partial \log P)_{\rm ad}$ is the adiabatic derivative with respect to the pressure P of the radiative conductivity $\chi = \frac{16\sigma T^3}{3\rho\kappa}$ (κ and σ are the opacity and Stefan-Boltzmann constant, respectively). The free parameter $\xi_{\rm PC}$ is of the order of unity but has to be calibrated from the observational constraints. We adopted here either $\xi_{\rm PC} = 0.0$ (reference set A, no penetration) or $\xi_{\rm PC} = 1.3$ (set K), this latter best adjusts the oscillatory behaviour of

- the individual frequency separations $rr_{01/10}(n)$ of HD 52265 (Lebreton & Goupil 2012).
- Rotation: We did not include rotational mixing in our models, except in one test case (see subset A in Appendix A), where we considered rotation and its effects on the transport of angular momentum and chemicals as described in Marques et al. (2013). In that case, additional free coefficients enter the modelling: a coefficient K_w intervenes in the treatment of magnetic braking by stellar winds (see Eq. 9 in Marques et al. 2013), following the relation by Kawaler (1988). We adjusted K_w so that the final model has the observed rotation period. This is one option among many possible ones. A thorough study of the impact of rotation on the modelling of HD 52265 will be presented in a forthcoming paper.
- Atmospheric boundary condition: The reference models are based on grey model atmospheres with the classical Eddington T-τ law. In set F, we investigated models based on the Kurucz (1993) T-τ law. For consistency with these Kurucz (1993) T-τ tables, in models F convection is computed according to the MLT theory.
- − Solar mixture: We adopted the canonical GN93 mixture $\overline{\text{(Grevesse \& Noels 1993)}}$ as the reference, but considered the AGSS09 solar mixture (Asplund et al. 2009) in set C. The GN93 mixture $(Z/X)_{\odot}$ ratio is 0.0244, while the AGSS09 mixture corresponds to $(Z/X)_{\odot} = 0.0181$.
- <u>Stellar chemical composition:</u> The mass fractions of hydrogen, helium and heavy elements are denoted by X, Y, and Z respectively. The present (Z/X) ratio is related to the observed [Fe/H] value through [Fe/H] = $\log(Z/X) \log(Z/X)_{\odot}$. We took a relative error of 11 per cent on $(Z/X)_{\odot}$ (Anders & Grevesse 1989). The initial $(Z/X)_{\odot}$ ratio is derived from model calibration, as explained below.
 - For the initial helium abundance Y_0 we considered different possibilities. When enough observational constraints were available, the value of Y_0 was derived from the optimization of the models. When too few observational constraints were available, the value of Y_0 had to be fixed. For the reference model, we derived it from the helium-to-metal enrichment ratio $(Y_0 Y_P)/(Z Z_P) = \Delta Y/\Delta Z$, where Y_P and Z_P are the primordial abundances. We adopted $Y_P = 0.245$ (e.g. Peimbert et al. 2007), $Z_P = 0$. and, $\Delta Y/\Delta Z \approx 2$, this latter from a solar model calibration in luminosity and radius. Other choices for Y_0 are considered in the study and presented in Appendix A.
- Miscellaneous: The impact of several alternate prescriptions for the free parameters is investigated and described in Appendix A.

3.2. Calculation of oscillation frequencies

We used the Belgium LOSC adiabatic oscillation code (Scuflaire et al. 2008) to calculate the frequencies. Frequencies and frequency differences were calculated for the whole range of observed orders and degrees. The observed and computed seismic indicators defined in Sect. 2 were derived consistently.

As mentioned in Sect. 2, near-surface effects are at the origin of an offset between observed and computed oscillation frequencies. We investigated the impact of correcting the computed frequencies from these effects. For that purpose, in some models (presented in Section 3.4 below), we applied to the computed frequencies, the empirical corrections obtained by

Table 2. Summary of the different sets of input physics considered for the modelling of HD 52265. As detailed in the text, the reference set of inputs denoted by REF is based on OPAL05 EoS, OPAL96/WICHITA opacities, NACRE+LUNA reaction rates (this latter only for $^{14}N(p,\gamma)^{15}O$), the CGM formalism for convection, the MP93 formalism for microscopic diffusion, the Eddington grey atmosphere, and the GN93 solar mixture and includes neither overshooting nor convective penetration or rotation. For the other cases we only indicated the input that is changed with respect to the reference. The colours and symbols in column 3 are used in Figs. 4 to 6 and in Fig. 9, but note that the colour symbols used in Fig. 3 are unrelated.

Set	Input physics	Figure symbol/colour
A	REF	circle, cyan
\boldsymbol{B}	convection MLT	square, orange
C	AGSS09 mixture	diamond, blue
D	NACRE for $^{14}N(p,\gamma)^{15}O$	small diamond, magenta
\boldsymbol{E}	no microscopic diffusion	pentagon, red
F	Kurucz model atmosphere, MLT	bowtie, brown
G	B69 for microscopic diffusion	upwards triangle, chartreuse
H	EoS OPAL01	downwards triangle, purple
I	overshooting α_{ov} =0.15 H_P	inferior, yellow
J	overshooting $M_{\rm ov,c} = 1.8 \times M_{\rm cc}$	superior, gold
K	convective penetration $\xi_{PC}=1.3H_P$	asterisk, pink

Table 3. Summary of the different cases considered for the modelling of HD 52265. A and M stand for age and mass.

Case	Observed	Adjusted	Fixed
1	$T_{\rm eff}$, L , [Fe/H]	A, M, $(Z/X)_0$	$\alpha_{\rm conv}, Y_0$
2a, b, c	$T_{\rm eff}$, L , [Fe/H], $\langle \Delta \nu \rangle$	A, M, $(Z/X)_0$, α_{conv}	Y_0
3	$T_{\rm eff}$, L , [Fe/H], $\langle \Delta \nu \rangle$, $\nu_{\rm max}$	A, M, $(Z/X)_0$, α_{conv} , Y_0	_
4	T_{eff} , L , [Fe/H], $\langle \Delta \nu \rangle$, $\langle d_{02} \rangle$	A, M, $(Z/X)_0$, α_{conv} , Y_0	_
5	T_{eff} , L , [Fe/H], $\langle r_{02} \rangle$, $\langle rr_{01/10} \rangle$	A, M, $(Z/X)_0$, α_{conv} , Y_0	_
6	T_{eff} , L, [Fe/H], $r_{02}(n)$, $rr_{01/10}(n)$	A, M, $(Z/X)_0$, α_{conv} , Y_0	_
7	$T_{\rm eff}, L, [{\rm Fe/H}], \nu_{n,\ell}$	A, M, $(Z/X)_0$, α_{conv} , Y_0	_

Kjeldsen et al. (2008) from the seismic solar model:

$$v_{n,l}^{\text{mod,corr}} = v_{n,l}^{\text{mod}} + \frac{a_{\text{SE}}}{r_{\text{SE}}} \left(\frac{v_{n,l}^{\text{obs}}}{v_{\text{max}}} \right)^{b_{\text{SE}}}, \tag{12}$$

where $v_{n,l}^{\rm mod,corr}$ is the corrected frequency, $v_{n,l}^{\rm mod}$ and $v_{n,l}^{\rm obs}$ are the computed and observed frequency, $b_{\rm SE}$ is an adjustable coefficient, $r_{\rm SE}$ is close to unity when the model approaches the best solution, and $a_{\rm SE}$ is deduced from the values of $b_{\rm SE}$ and $r_{\rm SE}$. We followed the procedure of Brandão et al. (2011). Kjeldsen et al. obtained a value of $b_{\rm SE,\odot}=4.9$ when adjusting the relation on solar radial modes frequencies. However, the value of $b_{\rm SE,\odot}$ should depend on the input physics in the solar model considered. Indeed, Deheuvels & Michel (2011) obtained $b_{\rm SE,\odot}=4.25$ for a solar model computed with the Cesam2k code and adopting the CGM instead of the MLT description of convection. Furthermore, $b_{\rm SE}$ can differ from one star to another. Under these considerations, we treated $b_{\rm SE}$ as a variable parameter of the modelling that we adjusted in the range [3.5, 5.5] so as to minimize the differences between observed and computed individual frequencies (see also Gruberbauer et al. 2012).

3.3. Model optimization

We used the Levenberg-Marquardt minimization method in the way described by Miglio & Montalbán (2005) to adjust the free parameters of the modelling so that the models of HD 52265 match at best observations, within the error bars. The goodness of the match is evaluated through a χ^2 -minimization. We calculated

$$\chi^2 = \sum_{i=1}^{N_{\text{obs}}} \frac{(x_{i,\text{mod}} - x_{i,\text{obs}})^2}{\sigma_{i,\text{obs}}^2}$$
 and $\chi_R^2 = \frac{1}{N_{\text{obs}}} \cdot \chi^2$, (13)

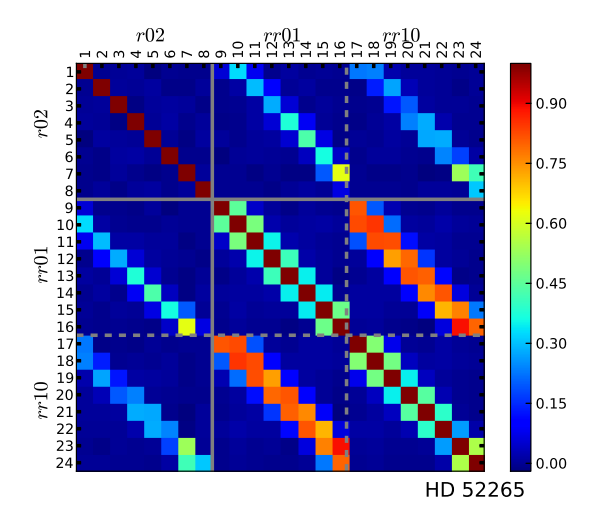


Fig. 2. Elements of the correlation matrix of the observed ratios $r_{02}(n)$ and $rr_{01/10}(n)$. Lines (columns) 1 to 8 correspond to the $r_{02}(n)$ ratios (n is in the range 17-24). Lines (columns) 9 to 16 correspond to the $rr_{01}(n)$ ratios and lines (columns) 17 to 24 correspond to the $rr_{10}(n)$ ratios (n is in the range 16-23). As expected, there are strong correlations between some of the data, in particular between the $rr_{01}(n)$ and $rr_{10}(n)$ ratios that have the same n value or values of n that differ by one unit.

where $N_{\rm obs}$ is the total number of observational constraints considered, $x_{\rm i,mod}$ and $x_{\rm i,obs}$ are the computed and observed values of the $i^{\rm th}$ constraint, respectively, and $\chi^2_{\rm R}$ is a reduced value. We distinguished $\chi^2_{\rm classic}$ based on the classical parameters and $\chi^2_{\rm seism}$ based on the seismic parameters. The more observational con-

straints available, the more free parameters can be adjusted in the modelling process. If too few observational constraints are available, some free parameters have to be fixed (see below). Accordingly, seven optimization cases were considered, as listed in Table 3 and described in Sect. 3.4 below.

In the cases where we considered the constraints brought by individual separations ratios $r_{02}(n)$ and $rr_{01/10}(n)$, we had to take into account the strong correlations between the ratios. To evaluate the correlations, we drew random samples of 20,000 values of each individual frequency, assuming the errors on the frequencies are Gaussian, and then we calculated the corresponding ratios and the associated covariance matrix C, displayed in Fig. 2. In this case, the χ^2 was calculated as

$$\chi^{2} = \sum_{i=1}^{N_{\text{obs}}} (x_{i,\text{mod}} - x_{i,\text{obs}})^{\text{T}} . C^{-1} . (x_{i,\text{mod}} - x_{i,\text{obs}}),$$
 (14)

where T denotes a transposed matrix (Press et al. 2002).

3.4. Choice of the set of observational constraints

We hereafter describe the various situations considered where $N_{\rm par}$ unknown parameters of a stellar model are adjusted to fit $N_{\rm obs}$ observational constraints. We considered the cases summarized in Table 3. For each case we made one model optimization with each set of input physics listed in Table 2. We recall that the mean values of the frequency separations —either observed or theoretical—mentioned in the following were computed in the same way, as explained in Sect. 2.2.4.

1. Case 1: Age and mass from classical parameters.

In this case, we assumed that the classical parameters alone are constrained by observation ($T_{\rm eff}$, present surface [Fe/H], L). We determine the mass M, age A, and initial metal-to-hydrogen ratio (Z/X) $_0$ required for the model to match these constraints. Since this gives three unknowns for three observed parameters, we made assumptions on the other inputs of the models, mainly the initial helium abundance Y_0 , the mixing length $\alpha_{\rm conv}$, and overshooting parameter $\alpha_{\rm ov}$. As a reference, we assumed that Y_0 can be derived from the helium-to-metal enrichment ratio $\Delta Y/\Delta Z=2$. We took $\alpha_{\rm conv,\odot}$ =0.688 from solar model calibration and $\alpha_{\rm ov}$ =0.0. Other models, presented in Appendix A, consider extreme values of Y_0 (the primordial, minimum allowed value, 0.245), of $\alpha_{\rm conv}$ (0.550, 0.826, i.e. a change in $\alpha_{\rm conv,\odot}$ by 20 per cent), and of $\alpha_{\rm ov}$ (0.30).

2. Cases 2a, b, c: Age and mass from large frequency separation $\langle \Delta \nu \rangle$ and classical parameters.

In case 2, we assumed that only $\langle \Delta \nu \rangle$ is known together with the classical parameters. We then adjusted the mixing-length parameter together with the mass, age, and initial metal-to-hydrogen ratio (four unknowns, four constraints). We still had to fix the initial helium abundance from $\Delta Y/\Delta Z$. We considered three sub-cases.

In sub-case 2a, we did not explicitly calculate the frequencies of the model but derived the model's large frequency separation from the scaling relation (Eq. 6) and compared this with the observed mean large frequency separation $\langle \Delta \nu \rangle$ of Table 1. In sub-case 2b, we estimated the theoretical $\langle \Delta \nu \rangle$ from the computed set of individual frequencies and compared it with the observed $\langle \Delta \nu \rangle$. In sub-case 2c, we adjusted the computed $\Delta \nu_{\rm asym}$ (Eq. 2) to the observed value in Table 1. In cases 2b and 2c, we corrected the model frequencies for near-surface effects according to Eq. 12.

3. Case 3: Age and mass from scaled values of $\langle \Delta \nu \rangle$ and ν_{max} , and classical parameters.

This case is similar to case 2a with the additional constraint on v_{max} from the scaling relation (Eq. 4). Frequencies are not explicitly calculated in this case.

4. Case 4: Age and mass from large frequency separation $\langle \Delta \nu \rangle$, mean small frequency separation $\langle d_{02} \rangle$, and classical parameters.

In this case the frequencies are explicitly calculated and corrected for near-surface effects according to Eq. 12. The model $\langle \Delta \nu \rangle$ and $\langle d_{02} \rangle$ are compared with the observed values of Table 1.

5. Cases 5 and 6: Age and mass from frequency separations ratios $-r_{02}$, $rr_{01/10}$ – and classical parameters.

In both cases the frequencies are explicitly calculated. In case 5, the mean values of r_{02} and $rr_{01/10}$ were calculated and compared with the observed values of Table 1. In case 6, we used the observed individual ratios $r_{02}(n)$, $rr_{01/10}(n)$ to constrain the models. Since the use of r_{02} , $rr_{01/10}$ allows us to minimize the impact of near-surface effects (Roxburgh & Vorontsov 2003), we used uncorrected ratios. On the other hand, we always accounted for observed data correlations. However, a model neglecting these correlations was calculated, which shows that they do not affect the results very much (see Appendix A). In the appendix, we also discuss the point made by Roxburgh & Vorontsov (2013) on the correct way to extract from a model the frequency separation ratios that are to be compared with observed ones.

6. Case 7: Age and mass from individual frequencies $v_{n,\ell}$ and classical parameters.

In this case, we considered the full set of 28 frequencies as constraints and corrected the model frequencies according to Eq. 12, where we adjusted b_{SE} to minimize the χ^2 . In Appendix A, we evaluated the differences obtained when no correction for near-surface effects was applied or when the surface effects are corrected using the Kjeldsen et al. (2008) solar value of the b_{SE} parameter ($b_{SE,\odot} = 4.90$).

4. Results of à la carte stellar modelling

The inputs and results of the different models presented in Sect. 3 are listed in Tables 4 and 5 for the reference models (set *A*, Table 2). Table 4 lists the quantities that are common main inputs of stellar models and can be determined by the optimization -or not-depending on the number of available observational constraints (see Table 3). Table 5 lists quantities that are common outputs of a model calculation, some of them may also be observational constraints. For clarity, we chose to present more results in Appendix A. In Tables A.1, A.2, and A.3, the results of the model optimization for different options in calculating reference models of set *A* are given. In Tables A.4 and A.5, the results of the model optimization for the input physics listed in Table 2 are presented.

The reduced values (χ^2_R) are also given to show the goodness of the match. Depending on the optimization case, there may be orders of magnitude differences in the χ^2_R -values. For instance, in case 1, the χ^2_R -values are very low because it is quite easy to find a model that matches the classical parameters alone. Hence, in case 1, for a given set of input physics and fixed free parameters, the optimization provides a very precise solution but the stellar model may not be accurately determined. The adopted values of the fixed parameters such as the mixing length may not be appropriate for the studied star; that introduces biases that can have strong impact on the results, as discussed below. Conversely, in

Table 4. Model results for the reference physics (set A, different cases, see Sect. 3 and Tables 2 and 3). The uncertainties result from the Levenberg-Marquardt minimization procedure (i.e. diagonal terms of the covariance matrix of inferred parameters). No uncertainty is indicated when the parameter has not been inferred but fixed (to few observational constraints as in cases 1 and 2a, b, c). Note that for the sake of homogeneous tables here and in Appendix A, we give a column listing the values of α_{ov} and ξ_{PC} although there are equal to 0 in reference set A.

Model	Age (Gyr)	M/M_{\odot}	$(Z/X)_0$	Y_0	$lpha_{ m conv}$	$\alpha_{ m ov}$ / $\xi_{ m PC}$	$b_{ m SE}$	$a_{\rm SE}/r_{\rm SE}$	$\chi^2_{\rm R,classic}/\chi^2_{\rm R,seism}$
A1	2.90 ± 1.09	1.18 ± 0.02	0.0483±0.0051	0.311	0.688	0.00/0.00	_	_	$6.4 \ 10^{-7}/$ -
A2a	2.38 ± 0.88	1.19 ± 0.02	0.0493 ± 0.0049	0.312	0.596 ± 0.100	0.00/0.00	_	_	$1.3 \ 10^{-1} / 7.9 \ 10^{-5}$
A2b	1.81 ± 0.80	1.20 ± 0.02	0.0491 ± 0.0052	0.312	0.559 ± 0.093	0.00/0.00	5.5	-4.5/1.00	$1.2 \ 10^{-1}/2.6 \ 10^{-4}$
A2c	1.97 ± 0.90	1.20 ± 0.02	0.0486 ± 0.0053	0.311	0.575 ± 0.086	0.00/0.00	5.5	-4.3/1.00	$2.3 \ 10^{-1}/1.6 \ 10^{-3}$
A3	1.98 ± 1.05	1.23 ± 0.01	0.0487 ± 0.0055	0.298 ± 0.020	0.565 ± 0.102	0.00/0.00	_	_	$2.6 \ 10^{-1}/1.7 \ 10^{-2}$
A4	2.08 ± 0.27	1.13 ± 0.03	0.0509 ± 0.0055	0.350 ± 0.021	0.581 ± 0.024	0.00/0.00	5.5	-4.7/1.00	$2.4\ 10^{-3}/4.2\ 10^{-5}$
A5	2.17 ± 0.32	1.25 ± 0.05	0.0467 ± 0.0061	0.280 ± 0.038	0.671 ± 0.093	0.00/0.00	_	_	$3.3 \ 10^{-7} / 4.0 \ 10^{-3}$
A6	2.21 ± 0.11	1.22 ± 0.02	0.0502 ± 0.0024	0.299 ± 0.011	0.599 ± 0.031	0.00/0.00	_	_	$1.7 \ 10^{-1} / 8.5 \ 10^{-1}$
A7	2.17 ± 0.02	1.27 ± 0.00	0.0486 ± 0.0007	0.274 ± 0.001	0.601 ± 0.004	0.00/0.00	4.2	-5.1/1.00	$5.3 \ 10^{-1}/1.7 \ 10^{0}$

Table 5. Model restitution of the chosen observational constraints plus quantities of interest. Models listed here were optimized with the reference physics (set A, different cases, see Sect. 3 and Tables 2 and 3). As explained in the text, in cases 2b, 2c, 4, and 7 the optimization considers individual frequencies and separations that were corrected for near-surface effects while in cases 5 and 6 the optimization is based on un-corrected separation ratios r_{02} and $r_{r_{01/10}}$. In case 1 no seismic constraints are considered. In cases 1, 5, and 6, we nevertheless chose to list below a corrected value of $\langle \Delta \nu \rangle$, i.e. a value corrected for surface effects a posteriori, after the optimized model was obtained. In cases 2a and 3, the scaling values of $\langle \Delta \nu \rangle$ are given, while in case 2c, we list $\Delta \nu_{\rm asym}$. Models without reference options are presented in the appendix.

Model	$T_{ m eff}$	L	[Fe/H]	$\log g$	R	$\langle \Delta \nu \rangle$	$\nu_{ m max}$	$\langle r_{02} \rangle$	$\langle rr_{01/10} \rangle$	X_C	$\Delta Y/\Delta Z$	$M_{\rm cc}$	$R_{\rm zc}$	$M_{\rm p} \sin i$
	[K]	$[L_{\odot}]$	[dex]	[dex]	$[R_{\odot}]$	$[\mu Hz]$	$[\mu Hz]$	_	_	_	_	$[M_{\star}]$	$[R_{\star}]$	$[\hat{M}_{ ext{Jupiter}}]$
A1	6116.	2.053	0.22	4.29	1.28	101.33	2127.	0.074	0.033	0.28	2.0	0.032	0.767	1.17±0.03
A2a	6050.	2.063	0.22	4.28	1.31	98.13	2061.	0.081	0.034	0.33	2.0	0.024	0.798	1.18 ± 0.03
A2b	6053.	2.063	0.22	4.28	1.31	98.14	2089.	0.088	0.035	0.40	2.0	0.019	0.819	1.19 ± 0.03
A2c	6067.	2.082	0.21	4.28	1.31	98.26	2083.	0.086	0.034	0.38	2.0	0.021	0.813	1.19 ± 0.03
A3	6024.	2.066	0.22	4.28	1.32	98.15	2086.	0.086	0.034	0.39	1.5	0.017	0.813	1.20 ± 0.03
A4	6110.	2.055	0.22	4.28	1.28	98.13	2035.	0.084	0.035	0.33	3.3	0.035	0.809	1.14 ± 0.03
A5	6116.	2.053	0.22	4.32	1.28	104.16	2253.	0.083	0.033	0.38	1.0	0.011	0.785	1.22 ± 0.05
A6	6043.	2.081	0.23	4.29	1.32	98.29	2095.	0.083	0.034	0.37	1.5	0.021	0.801	1.20 ± 0.03
A7	6020.	2.102	0.23	4.29	1.34	98.29	2124.	0.084	0.034	0.39	0.8	0.014	0.800	1.23±0.03

the other cases, seismology sets severe constraints on the models, which results in higher χ^2_R -values. The result is then less precise but the stellar model is more accurate. Note that at this point we listed all models regardless of their χ^2_R -value.

4.1. Observational constraints restitution

To each of the nine sets of observational constraints presented in Table 3 correspond 11 different models optimized with the input physics listed in Table 2. Figure 3 illustrates how the observational constraints of HD 52265 listed in Table 1 are reproduced by these models.

First, we examine the classical observables $T_{\rm eff}$, L, [Fe/H], and log g. We considered two diagrams, a $T_{\rm eff}$ -L and a [Fe/H]-log g diagram, as plotted in the upper left and right panels of Fig. 3. For the purpose of readability we distinguish each set in Table 3 but not the different input physics in Table 2. These latter are discussed in the next sections. The total size of these diagrams is the size of the 2σ error box on the classical parameters, while the inner box identifies the 1σ error box. The figures show that all models satisfy the classical constraints at the 2σ level with only two models lying outside the 1σ error box on $T_{\rm eff}$, L, [Fe/H], and log g. These outliers are model E6 ([Fe/H]=0.28, no microscopic diffusion) and model E6 (E6) and E60 (E6) and E61 (E6) and E63 (E6) and E64 (E6) and E65 (E6) and E65 (E6) and E66 (E60) are range of the observed spectroscopic effective

temperature. This supports the claim for a redetermination of the observed $T_{\rm eff}$ in the light of the seismic surface gravity, which is robust, as discussed below.

The seismic value for log g is found to be mostly independent of the model input physics (see also Sect. 4.4) and differs from the spectroscopic one by 0.03 dex. Note that two models have a log g in the upper range of the spectroscopic error bar, that is higher and more different than the seismic value. These are the two models of case 5 with overshooting (I5 and J5). However, as discussed below, these models are not considered in the following (model I5 has a very low initial helium content, much lower than the primordial value, while model J5 has a high $\chi^2_{\rm R,seism}$).

Second, we examine the seismic mean observables $\langle \Delta \nu \rangle$, $\langle r_{02} \rangle$, and $\langle rr_{01/10} \rangle$. We considered two diagrams, a $\langle \Delta \nu \rangle - \langle r_{02} \rangle$ and a $\langle \Delta \nu \rangle - \langle rr_{01/10} \rangle$ diagram, as plotted in the lower left and right panels of Fig. 3. Here, the total size of these diagrams is the size of the 10σ error box on the seismic parameters, while two inner boxes delimit the 1σ and 3σ error boxes. We note that many models lie outside the 1σ error box of $\langle \Delta \nu \rangle$, $\langle r_{02} \rangle$, and $\langle rr_{01/10} \rangle$. Some models are not even in the plotted areas. In most of these cases, the seismic data have not been used as model constraints. In particular, no model of case 1 matches the seismic constraints. This shows that a model that only matches the classical parameters can indeed be very far from a seismic model.

We also note that several models in Tables 5, A.3, A.5 have ν_{max} -values well outside the 1σ range of the observational determination of Ballot et al. (2011) (we recall that case 3 models

have been optimized on ν_{max}). This can be explained by the fact that the error bar on ν_{max} given by Ballot et al. is an internal error that is quite small (1 per cent). As shown by Barban et al. (2013), the method adopted to infer ν_{max} from the power spectra affects its value. Furthermore, one can expect differences between the observational value of ν_{max} and the theoretical value, which obeys the scaling relation (e.g. Belkacem et al. 2013).

In the following, to derive the age and mass of HD 52265 and their uncertainties, we considered only the models that satisfy $\chi^2_{R,classic} < 1$. Because of the high precision of the frequencies, no model with $\chi^2_{R,seism} < 1$ was found. We therefore only kept models with $\chi^2_{R,seism} < 2$.

4.2. Age of HD 52265

Figure 4 (left panel) shows for each case in Table 3 the age of the optimal model for a given set of physics in Table 2.

In case 1 (2), Y and α_{conv} (Y) could not be inferred and had to be fixed by the modeller. Therefore, for these two cases, we calculated additional models with somewhat extreme choices of Y and α_{conv} . In case 1, we also included a model with much overshooting ($\alpha_{\text{ov}}=0.30$). These additional models, included in Fig. 4, are presented in Appendix A.2.

In case 1 (column 1 in Fig. 4), there is a large scatter in the ages of HD 52265 obtained with different sets of input physics when no seismic observations are available, that is $\approx \pm 60$ per cent with respect to the reference age. This is the usual situation of age-dating from classical parameters L, $T_{\rm eff}$ and surface [Fe/H]. The values of Y, α_{conv} , and α_{ov} had to be fixed and different ages result from different choices. In particular, for a change of $\alpha_{\rm conv}$ of 20 per cent around the solar calibrated value, the age changes by more than 50 per cent. At the highest boundary of the age interval, the oldest models are those without diffusion and the model with a long mixing length $\alpha_{conv} = 0.826$. The youngest models are models with the lowest -primordial- initial helium abundance ($Y_P = 0.245$) and the model with low $\alpha_{\rm conv} = 0.55$. The ages of the other models are concentrated in a narrow age interval, 2.6-3.0 Gyr, about that of reference model A.

We point out that if the error bars on the classical parameters were to be reduced, as will be the case after the Gaia-ESA mission (see e.g. Liu et al. 2012, and references therein), the error bar of an individual age determination with a given set of input physics would be reduced, but the scatter associated with the use of different input physics would remain the same unless significant advance in stellar modelling is made.

In cases 2a, b, and c, where the large frequency separation is included as a model constraint, the age scatter is smaller than in case 1. Unlike case 1, the ages of the optimal models computed with different input physics and free parameters span the whole range of the scattered interval. Indeed, the values of the inferred mixing length differ from one case to another and still span a wide range [0.466-0.656] for $\alpha_{\rm conv,cgm}$ for case 2a, for instance, as can be seen in Tables 4, A.2, and A.4. Moreover, the initial helium Y_0 slightly changes in the optimization because $\Delta Y/\Delta Z$ is fixed but Z/X is adjusted in the optimization. Note that for given input physics and free parameters (cases 2a, 2b, 2c for set A in Tables 4), the age is significantly modified depending on the way the mean large frequency separation is computed; the changes are correlated with changes in the inferred mixinglength values. The scatter in the inferred mixing-length values, hence on the age, is smaller when $\langle \Delta \nu \rangle$ is calculated explicitly (i.e. not from the scaling relation) using the stellar models (cases 2b and 2c).

In case 3, the age scatter is slightly smaller than in case 2a. As already pointed out in Lebreton (2013), this is because the additional constraint on ν_{max} does not add much more knowledge on the age of the star.

Cases 4, 5, 6, and 7 all take into account seismic constraints directly sensitive to age, that is either the small frequency separation d_{02} , the frequency separation ratios r_{02} , $rr_{01/10}$, or the individual frequencies. The spectacular consequence is a reduction of the age scatter, as can be seen in Fig.4.

For case 4, considering the different possible options for the input physics of the stellar models, our criterion $\chi^2_{R,seism} \leq 2$ excludes the model without microscopic diffusion (model E4). Accordingly, the ages range between 2.02 ± 0.22 Gyr (model J4) and 2.22 ± 0.27 Gyr (model C4). This yields an age of 2.15 ± 0.35 Gyr, that is an age uncertainty of $\sim \pm 16$ per cent.

For case 5, considering the different possible options for the input physics of the stellar models, two models (15, 15) were excluded because their initial helium abundance Y_0 was found to be much lower than the primordial value Y_P . Accordingly, the ages range between 2.08 ± 0.25 Gyr (model D5) and 2.33 ± 0.40 Gyr (model E5). This yields an age of 2.28 ± 0.45 Gyr, which means an age uncertainty of $\sim \pm 20$ per cent. It is possible to reduce this scatter even more. Helioseismology has shown that microscopic diffusion must be included if one considers the Sun. This must also be true for solar-like stars like HD 52265: its mass is only slightly larger than the solar one and it has an extended convective envelope. Excluding the model without diffusion then yields an age in the range 2.08 ± 0.25 Gyr (model D5) - $2.28 \pm$ 0.31 Gyr (model C6), that is, an age of 2.21 ± 0.38 Gyr, i.e. an age uncertainty of $\pm 17\%$. Hence the main cause of scatter on the high side of the age interval here is microscopic diffusion (model E5) followed by the solar mixture (model C5). The low side of the age interval comes from the change of nuclear reaction rates (model D5). This shows that we start to reach the quality level of data that enables testing the microscopic physics in stars other than the Sun.

For case 6, considering the different possible options for the input physics of the stellar models, our criteria $\chi^2_{\rm R,classic} \leq 1$ and $\chi^2_{\rm R,seism} \leq 2$ exclude models 16, J6 and K6. Accordingly, the ages range between 2.21 ± 0.11 Gyr (model A6) and 2.46 ± 0.08 Gyr (model E6). This yields an age of 2.32 ± 0.22 Gyr, that is an age uncertainty $\sim \pm 9.5\%$. The main cause of scatter here is microscopic diffusion closely followed by the choice of the solar mixture: GN93 (model A6) versus AGSS09 (model C6). The range for the mixing-length value is [0.588, 0.606]. This range is considerably narrower than the one usually taken a priori to compute stellar models. Compared with the values we obtained from a calibration of a solar model with the input physics of reference set A ($\alpha_{\text{conv,cgm},\odot} = 0.688 \pm 0.014$), the values obtained for HD 52265 are lower than solar by 12 - 15 per cent. The results for the initial helium abundance are discussed in Sect. 4.3 below. We point out that the range of ages obtained in case 6 is quite close to that obtained in case 5. This can be understood by the fact that, as shown in Fig. 1, the mean value of $\langle rr_{01/10} \rangle$ is already a good indicator of the evolutionary state, at least if the classical parameters are also used to constrain the stellar mass and if the convective core is small. We therefore reach a similar accuracy in cases 5 and 6, but the precision on the individual ages is better in case 6, which is more constrained by the use of individual ratios. Furthermore, as discussed in Sect. 4.6, in case 6, the individual values $rr_{01/10}$ provide additional information on

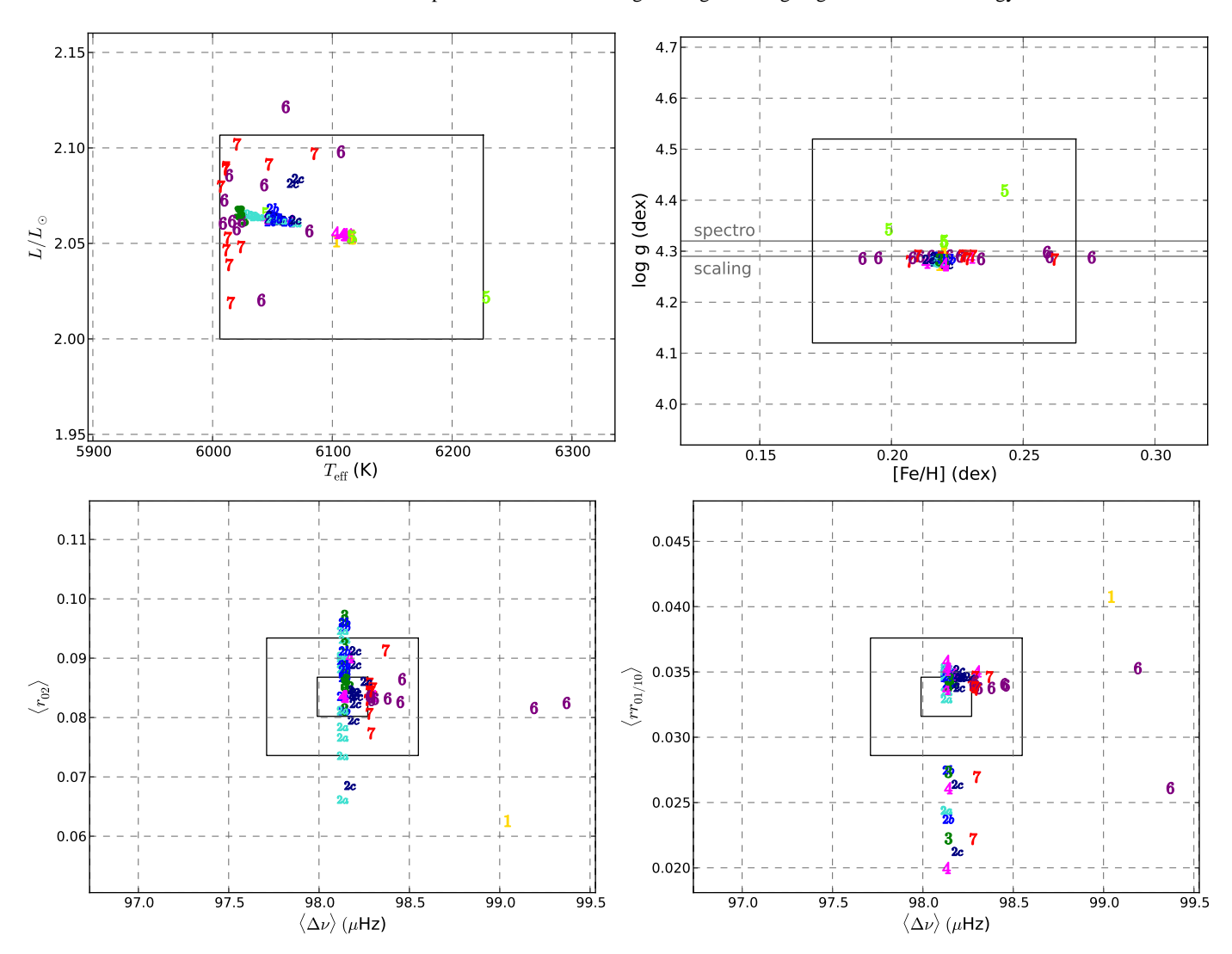


Fig. 3. Restoration of the observational constraints in the models. Upper figures are for classical parameters: H-R diagram (left), [Fe/H]-log g plane (right). The inner rectangle delimits the 1σ observational error bars, and the boundaries of the whole plotting area represent 2σ errors. Horizontal lines give the log g values of spectroscopy and seismic scaling. Lower figures are for seismic indicators: $\langle \Delta \nu \rangle - \langle r_{02} \rangle$ plane (left) and $\langle \Delta \nu \rangle - \langle r_{01/10} \rangle$ plane (right). Here, the rectangles delimit 1 and 3σ error bars, and the boundaries of the whole plotting area are 10σ errors. For each point, the symbol corresponds to the model number, as explained in Table 3. We used different colours to highlight the different cases (sets of observational constraints as defined in Table 3) at the basis of the modelling. Note that these colours are unrelated to the colours defined in Table 2 and used in Figs. 4 to 6, and in Fig. 9.

the star, unrelated to age. Their oscillatory behaviour, which is related to steep gradients of the sound speed, is an invaluable asset to characterize the depth of the convective envelope and the thermal and chemical structure at its radiative-convective interface (Lebreton & Goupil 2012). However, HD 52265 is a case study, with a small convective core, and we can expect that larger convective cores whose size is crucial for the age-dating are better characterized by individual ratios than by their mean values.

For case 7, considering the different possible options for the input physics of the stellar models, our criterion $\chi^2_{\rm R,seism} \leq 2$ excludes several models (E7, I7, I7, I7). Accordingly, the ages range between 2.05 ± 0.02 Gyr (model I8) and I80.249 I81. This yields an age of I82.27 I81. Gyr, that is an age uncertainty I82.5%. The upper boundary of the age interval is due to the choice of the MLT approach for the convective transport (model I87) closely followed by the choice of the solar mixture (model I87). The lower boundary is due to changes in the nuclear rates (model I87).

To summarize, the best precision and accuracy, in the context of the present input physics, is therefore obtained in case 4 -constrained by the mean values of the large and small frequency separations, case 6 -constrained by the individual values of the frequency separation ratios, and case 7 -constrained by individual frequencies. However, as stressed above, cases 4 and 7 suffer from the caveat that the individual frequencies were corrected for surface effects. As can be seen from model A7-noSE in Appendix A, the age is increased by more than 40 per cent in a model optimized without correcting for these effects. We therefore consider that case 6 is the optimal choice of observational constraints regarding the age of the star (see also the discussion by Silva Aguirre et al. 2013).

Additional models, based on different choices for the optimization (correction from surface effects, correlations between the seismic ratios, etc.), do not imply drastic changes in the optimized age (see Appendix A.2).

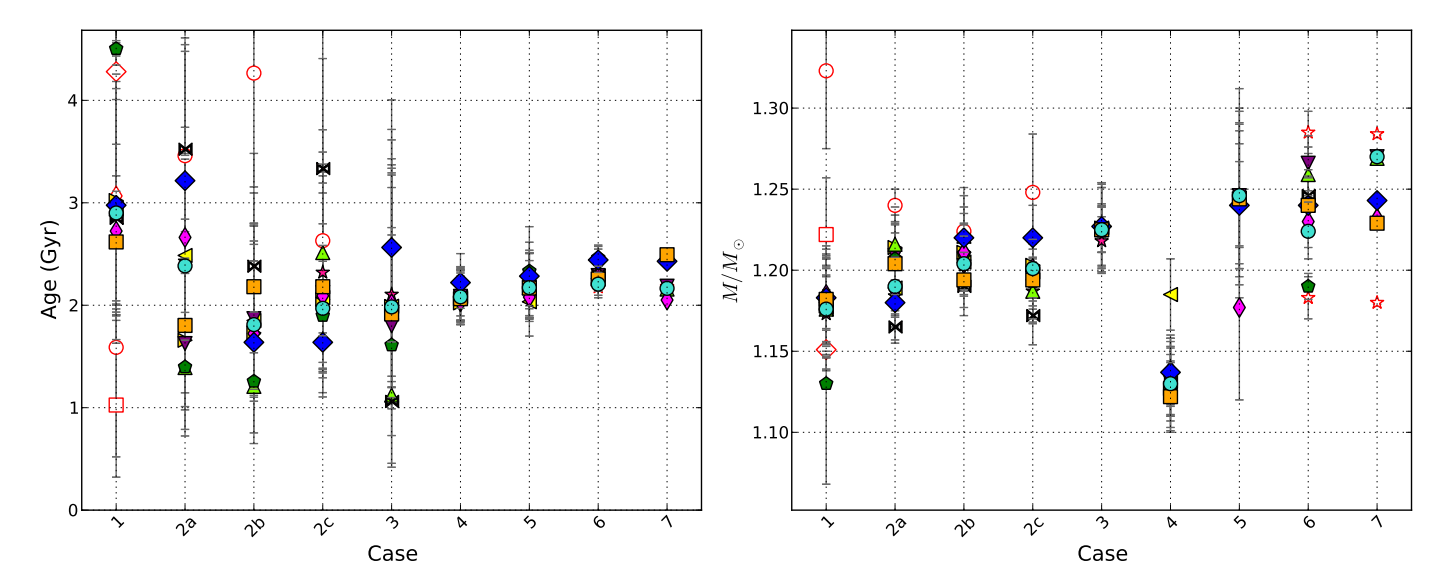


Fig. 4. Ranges of ages (left) and masses (right) derived from stellar model optimization for HD 52265. In the abscissae, we list the case numbers as defined in Table 3. For each case, several model optimizations can be identified according to the symbols and colours indicated in Table 2. In addition, open red symbols are for additional models of set A described in Table A.1 of Appendix A.2: circles are for different, low Y_0 values, square and diamond are for low and high α_{conv} values, small diamonds for models with large core overshooting. Red stars illustrate the Y_0 -M degeneracy in cases 6 and 7, but the inferred range is the same for all cases.

Degeneracy between age and mixing length: Figure 5, left panel, shows the relation between the convection parameter $\alpha_{\rm conv}$ and age of the optimized models. There is a possible trend for $\alpha_{\rm conv}$ to increase with age. From a linear regression we derived $\alpha_{\rm conv}/\alpha_{\rm conv,\odot} \simeq 0.13\times A+0.59$, where the age is in Gyr. This trend can be understood as follows: higher ages on the MS would imply lower $T_{\rm eff}$ and larger radii. The radius of a star is smaller for a more efficient convective energy transport. Smaller radii, hence higher $\alpha_{\rm conv}$ –related to more efficient convection— are therefore needed to bring $T_{\rm eff}$ back into the observational range. However, we checked that the ages determined by model optimization in cases 6 and 7 are not affected by this possible degeneracy because allowed variations of $\alpha_{\rm conv}$ along the regression line are limited by the constraints on $T_{\rm eff}$ and [Fe/H].

4.3. Mass and initial helium abundance

Figure 4, right panel shows for each case in Table 3 the mass of the optimal model for a given set of physics in Table 2. Like the age, the mass is better constrained when seismic data are taken into account, in particular when seismic constraints explicitly sensitive to mass are used (large frequency separation, frequency at maximum power as in cases 2 and 3).

Optimization of models of case 3 relies on the scaling-relations (Eqs. 4 and 6). These models therefore have the peculiarity that their mass and radius are tightly fixed because scaling relations provide quite precise values of the mass and radius. On the one hand, the accuracy of the derived values for the mass and radius depend on the accuracy of the scaling relations. As proposed in Sect. 4.2, models of case 6, optimized with the frequency separation ratios, provide the best age but since they do not constrain surface layers, they do not explicitly fix the mass. On the other hand, the ages of models of case 7 are less secure because they are affected by the correction for surface effects. Nevertheless, as can be seen from model A7-noSE in Appendix A.2, correction for surface effects only slightly modifies the optimized mass. Thus, we suggest that models of case

7, optimized with the individual frequencies, are probably more suitable for mass determination.

Degeneracy between mass and initial helium abundance: Figure 5, right panel, shows the relation between the initial helium abundance Y_0 and mass M of the optimized models. Like in Baudin et al. (2012), a clear anti-correlation between Y_0 and M is found. The lower Y_0 , the higher M. From a linear regression, we derived $Y_0 \simeq -0.58 \times M/M_{\odot} + 1.00$ with a scatter about this mean value of less than ± 0.02 .

This Y_0 -M degeneracy agrees with what is expected from homology relations (see e.g. Cox & Giuli 1968). For a MS star in the domain of mass of HD 52265, the luminosity varies as $L \propto \mu^{7.5} M^{5.5} R^{-0.5}$ with $R \propto \mu^{0.55} M^{0.73}$ (CNO cycle) or $R \propto \mu^{-0.43} M^{0.14}$ (pp chain). In addition, for a fully ionized gas, $\mu \approx 4/(8-5Y-6Z)$, which increases with Y. Therefore, for a given observed luminosity -fixed in the optimization process- there is a range of pairs (Y_0 , M) that lead to the same L value. The Y_0 -M degeneracy may severely hamper the determination of the mass of HD 52265, as shown by the results of cases 4 and 5. A large scatter in the mass value is obtained. However, low-mass models such as those found in case 4 have high values of Y_0 (i.e. higher than 0.33), which are hardly acceptable. More reasonable Y_0 values (i.e. lower than 0.30) would yield models with masses larger than $1.20 M_{\odot}$.

For set A, cases 6 and 7, we calculated additional optimized models with different (Y_0, M) pairs. Results are given in Appendix A.2 and appear as open red stars in the different figures. For our preferred case 7, taking into account the Y_0 -M degeneracy and keeping Y_0 in the range 0.26-0.32, we found reference models of set A with masses in the range $1.18-1.28~M_{\odot}$ and $\Delta Y/\Delta Z$ in the range 0.4-2.3. The scatter in mass around the central value is of ~ 5 per cent. In addition, for a given model, changing the physics would induce a mass scatter of about $0.04~M_{\odot}$ (~ 3 per cent). We note that, as is found in solar modelling, models C optimized with the AGSS09 solar mixture show a trend towards lower Y_0 , related to their lower metallicity. Other impacts of the Y_0 -M degeneracy are discussed below.

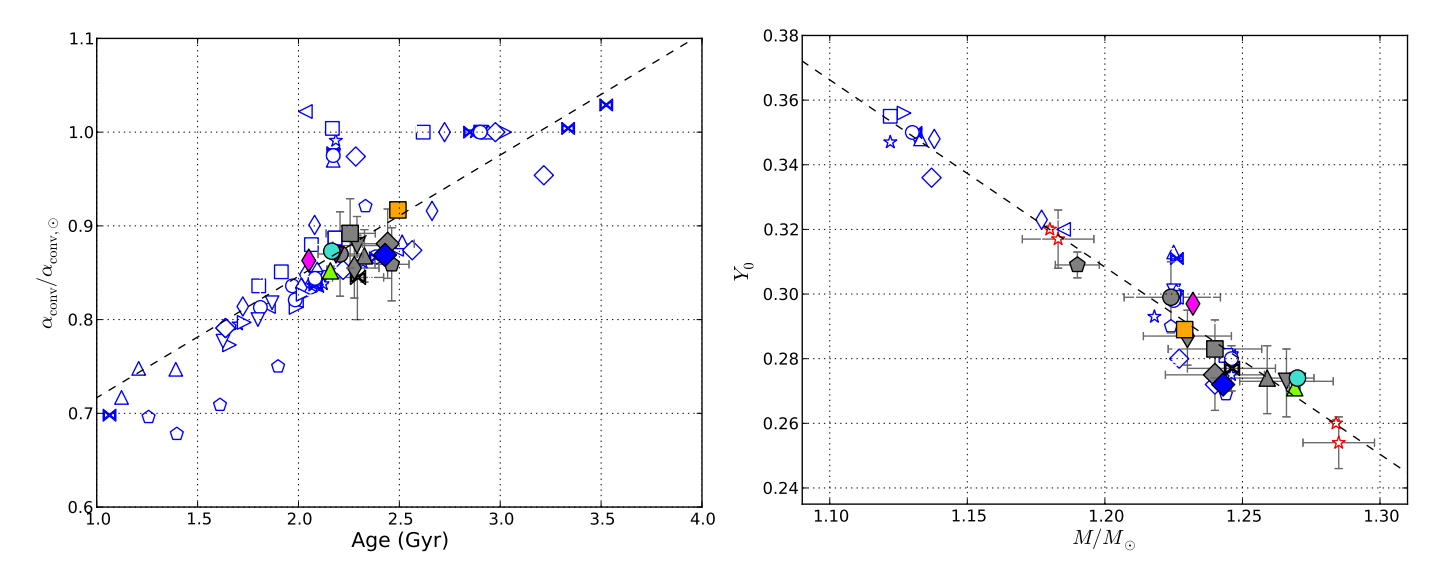


Fig. 5. Left: relation between the convection parameter α_{conv} and the age. To compare models, we expressed α_{conv} in units of the solar value, which, as mentioned in Sect. 3.1, mainly depends on the convection theory used in the model, i.e. $\alpha_{\text{conv},\odot,\text{cgm}} = 0.688$ and $\alpha_{\text{conv},\odot,\text{mlt}} = 1.762$. The regression line is $\alpha_{\text{conv}}/\alpha_{\text{conv},\odot} \simeq 0.13 \times A + 0.59$ (A in Gyr.). Colour symbols are for case 7 models (symbols and colours are listed in Table 2), grey symbols for case 6, and open blue for other cases. Right: relation between the initial helium abundance and the mass of HD 52265, as inferred from model optimization. The regression line is $Y_0 \simeq -0.58 \times M/M_\odot + 1.00$. Open red stars illustrate the impact of the Y_0 -M degeneracy (Table A.1).

4.4. Radius and surface gravity

Figure 3 (top, left) shows that the range of surface gravities of the models is very narrow, which means that log g is very well determined by the modelling and is hardly sensitive to the input physics (see also the determinations of the seismic surface gravities of Kepler stars by Mathur et al. 2012; Metcalfe et al. 2012). For HD 52265, taking into account the Y_0 -M degeneracy, seismic models of cases 6 and 7 have log g in the range 4.28 – 4.32, which improves the precision on log g by a factor of ten with respect to spectroscopy. We point out that for this star, the central value of the spectroscopic log g $(4.32 \pm 0.20 \, \text{dex})$ agrees well with both the value inferred from the scaling relation $(4.29 \pm 0.01 \text{ dex})$ and our seismic optimized value (4.30 ± 0.02) . This would not be the case for all the stars. The potential of asteroseismology to improve the determination of surface gravity and therefore of spectroscopic parameters ($T_{\rm eff}$, [Fe/H]) has already been demonstrated. For instance, it has been applied to the spectroscopic analysis of two CoRoT targets by Morel et al. (2013), and proposed for the calibration of log g of Gaia stars by Creevey et al. (2013).

The results for the star radius are shown in Fig. 6. Interestingly, all models have a radius in-between the Stefan-Boltzmann radius $R_{\rm SB}=1.28\pm0.06~R_{\odot}$ and the scaling radius $R_{\rm sc}=1.33\pm0.01~R_{\odot}$. Three groups of models lie on the Stefan-Boltzmann line. There are case 1 models —which is expected because they were optimized with only the classical parameters—and nearly all models of case 4 and 5. In the optimization process, these latter reproduce the observed effective temperature and luminosity of HD 52265 best. Case 6 and case 7 models with different input physics and accounting for the the Y_0 -M degeneracy, have seismic radii in the range $1.30-1.34~R_{\odot}$. This represents a precision of $\approx\pm1.5$ per cent on the radius, which is a good improvement on what can be obtained with the Stefan-Boltzmann law ($\approx\pm5$ per cent) for HD 52265.

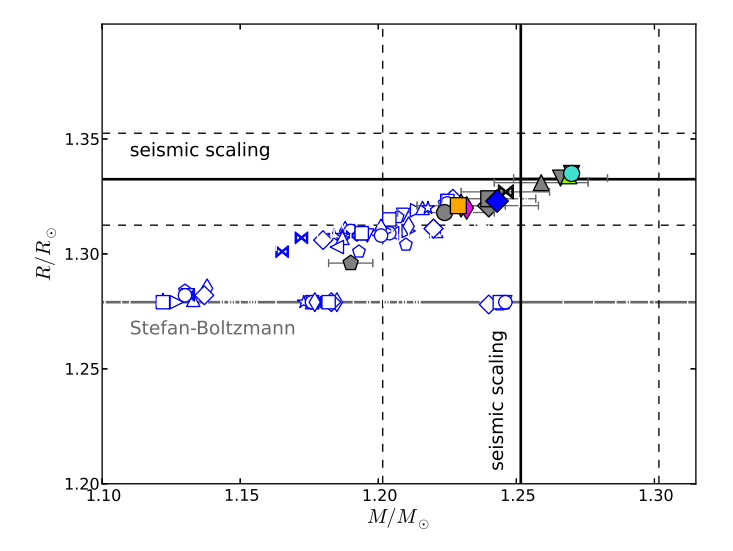


Fig. 6. Relation between the radius and the mass of HD 52265, as inferred from model optimization. Colours are for optimized models of case 7 of Table 3 for different input physics, as listed in Table 2. Models for case 6 are plotted in grey, other cases are shown with open blue symbols. Bold solid horizontal and vertical black lines represent the values of the mass and radius derived from the scaling relations (Sect. 2.2.2). The corresponding uncertainties are displayed with dashed lines. The radius obtained using the Stefan-Boltzmann relation (Sect. 2.1) is shown as a triple-dot dashed line. Three groups of models lie on the Stefan-Boltzmann line: case 1, 4, and 5 models, as discussed in the text.

4.5. Internal structure

HD 52265 has a very small convective core and a convective envelope. For instance, in model A7, the convective core has a mass $M_{\rm cc} \sim 0.014~M_{\star}$ and a radius $R_{\rm cc} \sim 0.045~R_{\star}$, while the

radius at the basis of the convective envelope is $R_{\rm zc} \sim 0.80~R_{\star}$. These quantities can be quite different in other models, which are nevertheless seismically equivalent. In particular, the Y_0 -M degeneracy has a major impact on the core mass. For instance, changing Y_0 from 0.26 to 0.32 changes M_{\star} from 1.28 to 1.18 M_{\odot} , $M_{\rm cc}$ from 0.006 to 0.023 M_{\star} , and $R_{\rm cc}$ from 0.035 to \sim 0.053 R_{\star} . The depth of the convective envelope is unaffected.

Models optimized with rather high, currently accepted or predicted values of core overshooting (sets I and J) show quite high values of $\chi^2_{R,seism}$, indicating that overshooting is probably ruled out for this star. We investigated this point in depth by performing an optimization where we also adjusted the overshooting parameter (models A6-ov and A7-ov, in the appendix). We found that quite low overshooting is indeed preferred, with $\alpha_{\rm ov}$ in the range 0.0 – 0.04. In principle, seismology has the potential to distinguish between different values of overshooting even for small cores through the signature left in the oscillation spectrum by the convective core (see the recent works by Silva Aguirre et al. 2013; Brandão et al. 2013, and references therein). Such diagnostics are beyond the scope of this paper. However, we made some additional tests that indicate that in the case of HD 52265, the seismic data are probably not precise enough to allow us to infer the size of the mixed core precisely or accurately.

4.6. Seismic properties

In Fig. 7, we show how the stellar models succeed -or not- in matching observed oscillation frequencies and frequency separations. Since a thorough examination of seismic properties of all the models is beyond the scope of this paper, we selected some models. The top left panel shows the échelle diagram corresponding to the model of case A7, optimized on the basis of the individual frequencies. When surface effects are corrected for, the model succeeds rather well in reproducing the échelle diagram for a value of the adjustable parameter $b_{\rm SE} = 4.2$ (Eq. 12) compatible with the solar value obtained by Deheuvels & Michel (2011) with quasi-similar input physics $(b_{\rm SE,\odot} = 4.25)$. On the other hand, in the high-frequency range, un-corrected models do not match observations. In this respect, models A6 (frequencies not corrected, not plotted) and A7 (with uncorrected frequencies) give similar results. Furthermore, the top right panel shows that model A7 reproduces the observed individual large frequency separations $\Delta v_{\ell}(n)$ quite well. The bottom left panel shows the comparison of the observed and model frequency separation ratios $rr_{01/10}(n)$. Model A7 reproduces the mean slope of the variation of the ratios rather well, but not the oscillatory behaviour. As shown by Lebreton & Goupil (2012), this behaviour in HD 52265 is reproduced in models that include convective penetration below the convective envelope, like the model of set K, which is similar to set A but with $\xi_{PC} = 1.3$. The figure also shows the effect of the Y_0 -M degeneracy on the diagram. The larger the helium abundance, the higher the $rr_{01/10}(n)$ ratios. However, with the present accuracy on the data, it is hard to distinguish the models with different (Y_0, M) values. Finally, we plotted a model of set I that takes into account a moderate amount of core overshooting ($\alpha_{ov} = 0.15$). As already pointed out in Section 4.5, the overshooting amount cannot be very large since even a moderate amount of overshooting is ruled out by the present data. The bottom right panel shows the fit of the $r_{02}(n)$ ratios. In this case, regarding the precision on the data, it is difficult to distinguish the models.

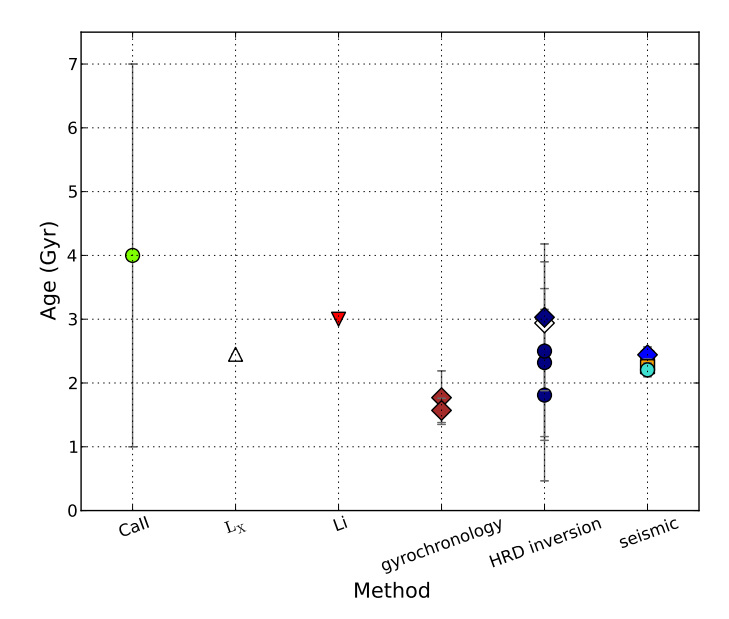


Fig. 8. Age estimates for HD 52265. Columns CaII, L_X , Li and gyrochronology give empirical estimates based on the R'_{HK} index (circle), the lower limit from X-luminosity (upwards triangle), the upper limit from lithium surface abundance (downwards triangle) and, the gyrochronology (diamonds). The column HRD inversion shows estimates based on inversion of isochrones with circles for Padova isochrones and diamonds for BaSTI isochrones, full symbols for Bayesian methods, and empty symbol for χ^2 -minimisation, see text. The column seismic shows the seismic determination for à la carte models of case 6 (Table 3 and Fig. 4)

5. Ages from other methods

We estimate below the age of HD 52265, on the basis of other age-dating methods (empirical or H-R diagram inversion). We compare the resulting ages with the age inferred from à la carte stellar modelling.

5.1. Empirical ages

5.1.1. Activity

The chromospheric activity and age of solar-type dwarfs appear to be anti-correlated. Empirical relations allow us to rely the CaII H & K emission index $R'_{\rm HK} = L_{\rm HK}/L_{\rm bol}$ to age (see e.g. Mamajek & Hillenbrand 2008, for a recent calibration). For HD 52265, values of $\log R'_{\rm HK}$ listed in the literature are in the range [-5.02, -4.59]. These low values indicate very low chromospheric activity. Using the Mamajek & Hillenbrand $R'_{\rm HK}$ -age relation, we derived an age of 4.0 ± 3.0 Gyr. The ages can also be roughly estimated from the Mamajek & Hillenbrand relation between the fractional X-ray emission $R'_{\rm X} = L_{\rm X}/L_{\rm bol}$ and age. For HD 52265, Kashyap et al. (2008) derived an upper limit, $L_{\rm X} < 28.28$, which provides a lower age limit of 2.5 Gyr. Clearly, such empirical calibrations are too coarse to provide a reliable age of evolved stars with low chromospheric activity. Indeed, as recommended recently by Pace (2013), the use of chromospheric activity as a stellar clock should be limited to stars younger than about 1.5 Gyr.

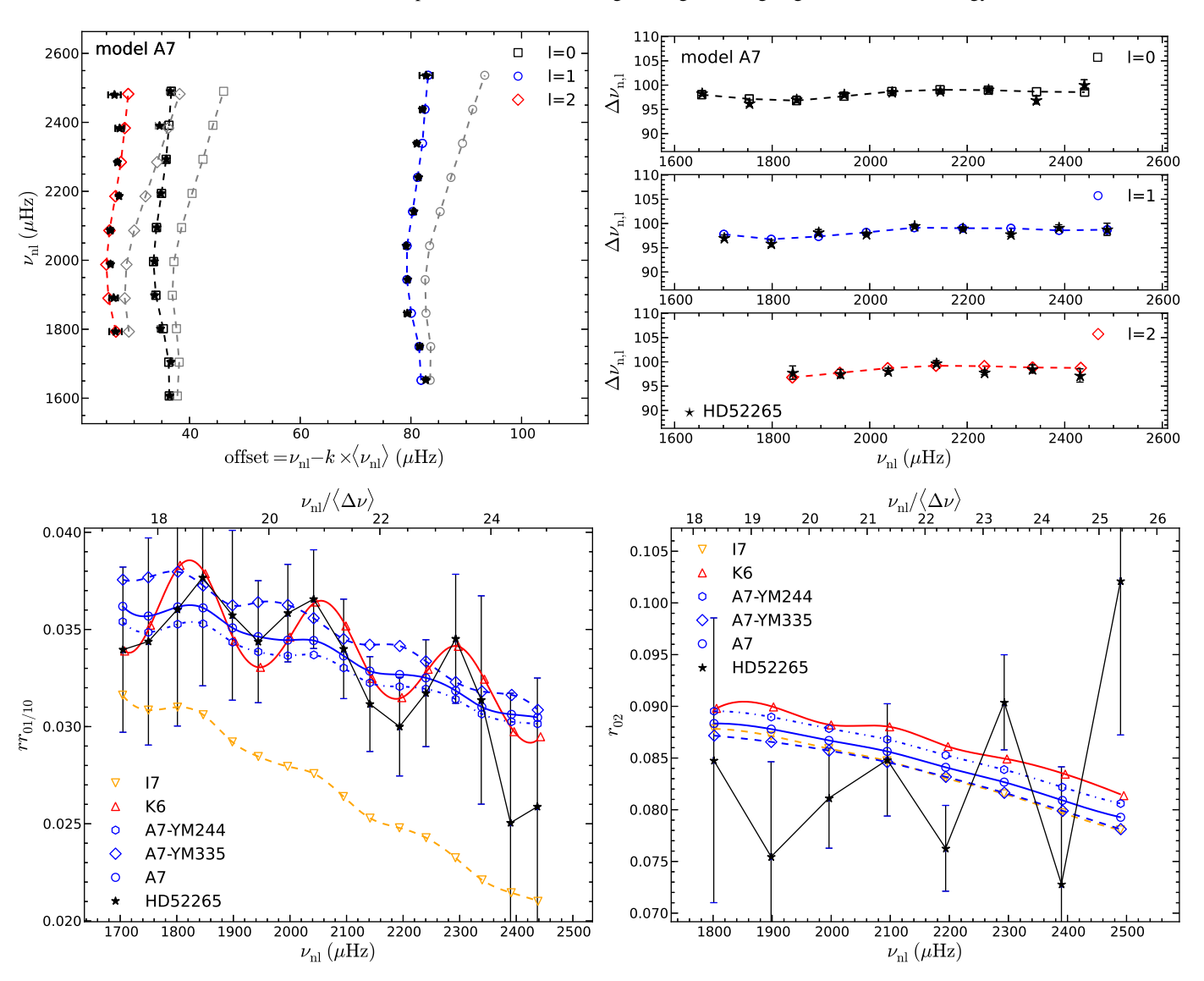


Fig. 7. Seismic properties of a selected set of models. *Top left panel*: échelle diagram for the best model A7, optimized on the basis of the individual frequencies and including -or not- the correction for surface effects. Star symbols represent the observed frequencies, while black squares, blue circles, and red diamonds denote the model frequencies for angular degrees $\ell=0,1$, and 2. In grey, we indicate the corresponding data before correction for surface effects. *Top right panel*: comparison of observed large frequency separations for case A7 (corrected frequencies). The symbols are the same as in the top right figure. *Bottom left panel*: comparison of the observed frequency separation ratios $rr_{01/10}(n)$ for a selected set of models, including the best model A7 (continuous blue line). Results for models A7-YM-244 (pentagons) and A7-YM335 (diamonds) illustrate the effect of the Y_0-M degeneracy. Results for model K6 (continuous red line) show the effect of including convective penetration below the convective envelope, while results for model I7 (dashed orange line) show the effect of a moderate overshooting of the convective core. *Bottom right panel*: same as in the bottom left figure, but for the $r_{02}(n)$ frequency separation ratios.

5.1.2. Photospheric lithium abundance

At the surface of low-mass stars, the lithium abundance can be depleted when the convective zone reaches the shallow regions where Li is destroyed by nuclear reactions at $T \approx 2.5 \times 10^6$ K or when mixing processes carry Li from the basis of the convective zone to the nuclear-burning region. A relation between the Liabundance, effective temperature, and age is observed (but not fully understood). We used the Li abundance curves as a function of $T_{\rm eff}$ published by Sestito & Randich (2005) for clusters of different ages and derived a lower limit of 2.5 Gyr on the age of HD 52265 from several published values of its surface Li abun-

dance (log $\epsilon_{Li} \in [1.67, 2.88]$). With log $\epsilon_{Li} = 2.40 \pm 0.06$ from Gonzalez et al. (2010), we found an age < 3 Gyr.

5.1.3. Gyrochronology

In the course of their evolution, solar-type stars lose angular momentum via magnetic braking due to their mass loss. It leads to a decrease of their rotation rate, first quantified by Skumanich (1972). Gyrochronology, as proposed by Barnes (2007), is a new method to derive the age of solar-type stars via an empirical relation linking their rotation period, colour, and age, $t_{\rm Myr}^n = P_{\rm days} \times a^{-1} \times ((B-V)-c)^{-b}$ where a, b, and c, are constants. The constants were calibrated on the Sun, nearby

field stars and clusters by Barnes (2007) and then revised by Mamajek & Hillenbrand (2008). We applied these relations to HD 52265 (P_{rot} =12.3±0.14 days, see Sect. 2) and found an age of 1.57 ± 0.19 Gyr with Barnes's values of a, b, and c and 1.77 ± 0.42 Gyr with the values of Mamajek & Hillenbrand.

5.2. Age from pre-calculated sets of model isochrones

This method consists of placing a star in an H–R diagram and of interpreting its position by means of a grid of pre-calculated theoretical isochrones or evolutionary tracks. It is widely used to age-date large samples of stars for Galactic evolution studies (see e.g. Casagrande et al. 2011, and references therein). Different inversion techniques can be used to extract the stellar age (and mass) from theoretical isochrones. However, in several regions of the H–R diagram, for instance when the star is close to the zero-age main-sequence (ZAMS) or at turn-off, the morphology of the isochrones is complex and leads to severe age degeneracy. To cope with these problems, Pont & Eyer (2004) and Jørgensen & Lindegren (2005) proposed to take a Bayesian approach, with several priors, in particular, one on the initial mass function.

Bayesian inversion techniques using the Padova isochrones give ages of 2.5 ± 1.4 Gyr (Holmberg et al. 2009) and 2.32 ± 1.16 Gyr (Casagrande et al. 2011). We also used the Girardi et al. (2002) and da Silva et al. (2006) PARAM web interface¹ and found an age of 2.81 ± 1.49 Gyr. On the other hand, from the use of BaSTI isochrones (Pietrinferni et al. 2004), Casagrande et al. obtained 3.03±1.15 Gyr. Still with BaSTI isochrones, using the tools developed by Guédé et al. (2013), we inferred 2.94 Gyr from a χ^2 -minimisation. As can be seen in Fig. 8, the ages obtained cover a wide range, 0.5-4.2 Gyr, because of the different isochrone grids and inversion methods used. For the star HD 52265, which is approximately half-way on its MS, we expect the isochrone inversion technique and the optimization performed in case 1 of the present study to be equivalent in terms of precision -for a given set of input physics- because they are both based on the observational constraints on the classical parameters. However, the isochrone grid to be used for the inversion has to be dense enough both in mass and chemical composition. On the other hand, for stars lying in regions of degeneracy in the H-R diagram, priors should be included in the optimization process in case 1 to deal with multiple possible solutions (see e.g. Jørgensen & Lindegren 2005).

5.3. Comparison of ages from different methods

In Fig.8, ages of HD 52265 obtained from different methods are compared. As discussed before, the ages from the $R'_{\rm HK}$ index, the X-luminosity, and the lithium surface abundance are not reliable for this star. The ages from gyrochronology are very precise but not accurate because gyrochronology is an empirical method that relies on calibrations (on solar, nearby stars, and cluster ages). As pointed out by D. Soderblom (2013, invited review talk at the International Francqui Symposium), seismic ages combined with precise rotation periods as provided by the *Kepler* or CoRoT missions will give the potential to more fully test and calibrate gyrochronology. Finally, there is a large scatter in the ages derived from H-R diagram inversion. This scatter is similar to that obtained in case 1 stellar modelling, when no seismic constraints are available. The à la carte seismic age-dating that we obtained in the present study is by far the most precise.

6. Age and mass of the exoplanet orbiting HD 52265

A first estimate of the mass of the exoplanet orbiting HD 52265 was proposed by Butler et al. (2000) using their RV measurements and Eq. 1. From a grid of stellar models, Butler et al. inferred the mass of the star, first by placing the star in a colour-magnitude diagram at solar metallicity, and then by correcting for the metallicity of the star –which they estimated to be [Fe/H] = 0.11, using stars of published mass and metallicity. They inferred a stellar mass of $1.13 \pm 0.03 M_{\odot}$ (note that the error bar here is an internal error bar and does not take into account the uncertainties of the stellar models) and deduced that the exoplanet has a mass $M_p \sin i = 1.13 \ M_{\rm Jupiter}$. They did not give uncertainties on this determination, nor the values for the age of the host-star.

Using the RV data reported by Butler et al. (2000) and isochrone fits to derive the mass of the host-star, Gizon et al. (2013) estimated the minimum mass of the exoplanet to be $M_{\rm p,min}=1.09\pm0.11~M_{\rm Jupiter}$ (i.e. $\sin i=1$ in Eq.1). Here, again, the error bar does not account for the uncertainties of stellar models. Furthermore, with their measure of the inclination of the spin axis of the star ($\sin i=0.59^{+0.18}_{-0.14}$), assumed to be the axis of the planetary orbit as well, they estimated the mass of the exoplanet to be $M_{\rm p}=1.85^{+0.52}_{-0.42}~M_{\rm Jupiter}$. Note that the dominant source of error is the $\sin i$ error.

We have re-estimated the exoplanet mass on the basis of the range of mass of the host-star discussed above. Figure 9 shows the range of mass of the exoplanet as a function of its age, assumed to be the age of the host-star, for the different physical options and optimization sets considered. When considering all cases, the scatter is quite large. In particular, models of case 4, which correspond to low stellar mass, form the bunch of points at low planet mass and at age around 2 Gyr, but note that these models have to be excluded because of their very high initial helium abundance. On the other hand, the use of seismic constraints in cases 6 and 7 considerably narrows the range of ages of the star while they mostly favour higher masses with respect to other cases (see Figs. 4). Hence, these optimized models predict a higher mass for the exoplanet. Taking into account the $Y_0 - M$ degeneracy and excluding models E without microscopic diffusion, the exoplanet mass $M_p \sin i$ is found to be in the range $1.16 - 1.26 M_{\text{Jupiter}}$, where we included the error budget due to the error on the host-star mass optimization and on the RV data characterizing the exoplanet orbit. The scatter around the central value is therefore ~ ±4 per cent. These values of the mass are higher (≈ 7 per cent) than the value of Butler et al. (2000). Furthermore, with the extreme values of $\sin i$ given by Gizon et al. (2013), the mass of the exoplanet would be in the range $1.5 - 2.8 M_{\text{Jupiter}}$. The scatter is slightly larger than that in the result by Gizon et al. because we accounted for the uncertainties in the stellar model inputs. We therefore confirm that the companion of HD 52265 is a planet, not a brown dwarf.

7. Conclusions

The optimization of models of the star HD 52265 using both classical and seismic observational data provides strong constraints on the age, mass, radius, and surface gravity of the star, and on the mass of its exoplanet. Taking into account the full information provided by seismic observations and considering the current uncertainties that affect the calculation of stellar models, we found an age A=2.10-2.54 Gyr, a mass $M/M_{\odot}=1.14-1.32$, a radius $R/R_{\odot}=1.30-1.34$, and a surface gravity log g=4.28-4.32.

http://stev.oapd.inaf.it/cgi-bin/param

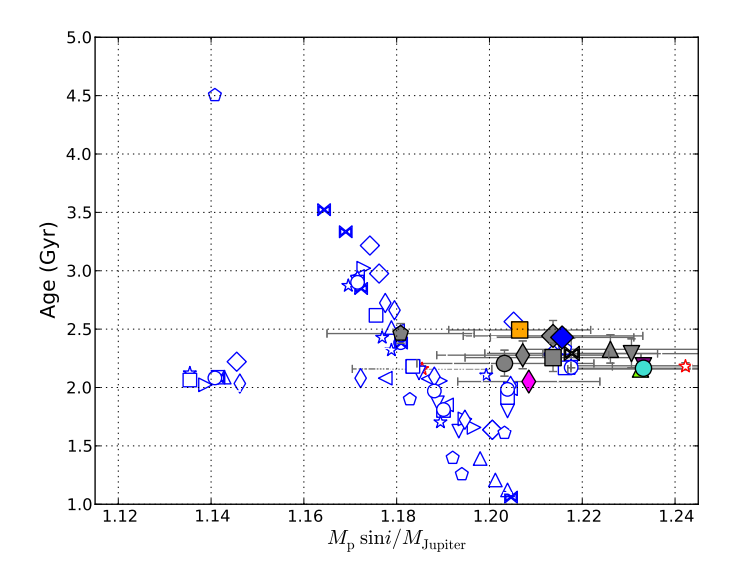


Fig. 9. Age and mass of the exoplanet $M_p \sin i$ inferred from the mass of its host star. Colours are for optimized models of case 7 of Table 3 for different input physics, as listed in Table 2. Models for case 6 are plotted in grey, other cases are shown with open blue symbols. The group of models with low mass and age of ~ 2 Gyr are case 4 models, to be rejected because of their high initial helium abundance (see text).

We stress that in the present case, the mass and radius given by the scaling relations agree quite well with the result of the full modelling. This can be explained by the fact that the effective temperature used in the scaling relations is accurately determined by spectroscopy and does correspond to the evolutionary stage of the star for its metallicity.

The mass of the exoplanet is found to be in the range $M_p \sin i = 1.16\text{-}1.26$ M_{Jupiter} . This represents considerable progress with respect to what can be achieved without seismic data or when using only mean values inferred from seismic observations, as the mean frequency separation and frequency at maximum power. An important point is that while the age, mass, and radius of the star can be rather well estimated from classical and mean seismic parameters after the input physics of the models are fixed, uncertainties on the input physics produce a large scatter of the results. We demonstrated here that taking full profit of seismic data -in particular considering the frequency separation ratios- considerably reduces this scatter by allowing one to estimate free parameters of the models.

The full optimization performed here allowed us to better estimate the uncertainties and identify their origin, in particular concerning the age.

When no seismic constraints are available, the main cause for the age scatter and inaccuracy are the values of the mixing length and initial helium abundance that belong to a wide interval of possible values. Seismic constraints allowed us to estimate these free parameters of stellar models, as the mixing-length parameter for convection and the core overshoot and convective penetration parameters. As a result, the interval of possible values for $\alpha_{\rm conv}$, [0.59, 0.61], is considerably narrowed. These values are lower by 12 – 15 per cent than the solar values obtained by a solar calibration using the same input physics. This provides an observational constraint on the convective transport efficiency that can be compared with the results of 3-D numerical simulations. The initial helium abundance could also be obtained but there remains a degeneracy between helium and mass. To re-

move this degeneracy, more precise oscillation frequencies are required. As studied by Houdek & Gough (2007), it would allow us to detect an oscillatory behaviour of the frequencies that results from changes in the adiabatic exponent in the second helium ionization zone, a seismic diagnostic of the helium abundance. When the mixing length and initial helium abundance are unlocked, we find that the main cause of the age scatter is the choice of the solar mixture. When this problem is solved, we will then be at the level of testing nuclear reaction rates and internal transport processes, as demonstrated here.

Currently, the availability of precise observational frequencies for close well-known stars only concerns a small number of stars among which very few host an exoplanet. These calibrators are key to better understanding the physics that govern stellar interiors. A crucial need for the future is to increase the number of these calibrators. In this context, the ESA-PLATO high-precision photometry mission is really needed (Rauer et al. 2013). It will provide essential information that complements the classical data that will be provided, with ultra high accuracy, by the Gaia-ESA mission, and interferometry and spectroscopic ground-based observations. Obtaining numerous and precise asteroseismic data is also a necessary step to make towards the full characterization of the age, mass, and radius of exoplanets. It is only with this effort that we will achieve a new understanding of the interiors, habitability, and formation scenario of exoplanets and exoplanetary systems.

<u>Acknowledgements.</u> This research has made use of the SIMBAD database, operated at CDS, Strasbourg, France and of the NASA's Astrophysics Data System. We warmly thank Kévin Belkacem for his comments on the manuscript.

References

Anders, E. & Grevesse, N. 1989, Geochim. Cosmochim. Acta, 53, 197 Angulo, C., Arnould, M., Rayet, M., et al. 1999, Nuclear Physics A, 656, 3 Asplund, M., Grevesse, N., Sauval, A. J., & Scott, P. 2009, ARA&A, 47, 481 Audard, N. & Provost, J. 1994, A&A, 282, 73

Baglin, A., Auvergne, M., Barge, P., et al. 2002, in ESA Special Publication, Vol.
 485, Stellar Structure and Habitable Planet Finding, ed. B. Battrick, F. Favata,
 I. W. Roxburgh, & D. Galadi, 17–24

Baglin, A., Michel, E., & Noels, A. 2013, in Astronomical Society of the Pacific Conference Series, Vol. 479, Astronomical Society of the Pacific Conference Series, ed. H. Shibahashi & A. E. Lynas-Gray, 461

Ballot, J., Gizon, L., Samadi, R., et al. 2011, A&A, 530, A97

Barban, C., Beuret, M., Baudin, F., et al. 2013, Journal of Physics Conference Series, 440, 012031

Barnes, S. A. 2007, ApJ, 669, 1167

Baudin, F., Barban, C., Goupil, M. J., et al. 2012, A&A, 538, A73

Belkacem, K., Goupil, M. J., Dupret, M. A., et al. 2011, A&A, 530, A142

Belkacem, K., Samadi, R., Mosser, B., Goupil, M.-J., & Ludwig, H.-G. 2013, in Astronomical Society of the Pacific Conference Series, Vol. 479, Astronomical Society of the Pacific Conference Series, ed. H. Shibahashi & A. E. Lynas-Gray, 61

Böhm-Vitense, E. 1958, ZAp, 46, 108

Brandão, I. M., Cunha, M. S., & Christensen-Dalsgaard, J. 2013, MNRAS Brandão, I. M., Doğan, G., Christensen-Dalsgaard, J., et al. 2011, A&A, 527, A37

Brown, T. M., Christensen-Dalsgaard, J., Weibel-Mihalas, B., & Gilliland, R. L. 1994, ApJ, 427, 1013

Burgers, J. M. 1969, Flow Equations for Composite Gases

Butler, R. P., Vogt, S. S., Marcy, G. W., et al. 2000, ApJ, 545, 504

Canuto, V. M., Goldman, I., & Mazzitelli, I. 1996, ApJ, 473, 550+

Casagrande, L., Schönrich, R., Asplund, M., et al. 2011, A&A, 530, A138

Chaplin, W. J., Basu, S., Huber, D., et al. 2014, ApJS, 210, 1

Chaplin, W. J. & Miglio, A. 2013, ARA&A, 51, 353

Christensen-Dalsgaard, J. 1988, in IAU Symposium, Vol. 123, Advances in Helio- and Asteroseismology, ed. J. Christensen-Dalsgaard & S. Frandsen, 295

Cox, J. & Giuli, R. 1968, Principles of Stellar Structure, vol I & II (Gordon & Bretch, New-York)

Creevey, O. L., Thévenin, F., Basu, S., et al. 2013, MNRAS, 431, 2419

da Silva, L., Girardi, L., Pasquini, L., et al. 2006, A&A, 458, 609

Deheuvels, S. & Michel, E. 2011, A&A, 535, A91

Escobar, M. E., Théado, S., Vauclair, S., et al. 2012, A&A, 543, A96

Ferguson, J. W., Alexander, D. R., Allard, F., et al. 2005, ApJ, 623, 585

Formicola, A., Imbriani, G., Costantini, H., et al. 2004, Physics Letters B, 591,

Freeman, K. C. 1993, in Astronomical Society of the Pacific Conference Series, Vol. 49, Galaxy Evolution. The Milky Way Perspective, ed. S. R. Majewski, 125

Gilliland, R. L., Marcy, G. W., Rowe, J. F., et al. 2013, ApJ, 766, 40

Gilliland, R. L., McCullough, P. R., Nelan, E. P., et al. 2011, ApJ, 726, 2

Gilmore, G. 1999, Baltic Astronomy, 8, 203

Girardi, L., Bertelli, G., Bressan, A., et al. 2002, A&A, 391, 195

Gizon, L., Ballot, J., Michel, E., et al. 2013, Proceedings of the National Academy of Science, 110, 13267

Gonzalez, G., Carlson, M. K., & Tobin, R. W. 2010, MNRAS, 403, 1368

Gough, D. O. 1990, in Lecture Notes in Physics, Berlin Springer Verlag, Vol. 367, Progress of Seismology of the Sun and Stars, ed. Y. Osaki & H. Shibahashi, 283

Grevesse, N. & Noels, A. 1993, in Origin and Evolution of the Elements, ed. N. Prantzos, E. Vangioni-Flam, & M. Casse, 15–25

Gruberbauer, M., Guenther, D. B., & Kallinger, T. 2012, ApJ, 749, 109

Guédé, C., Lebreton, Y., Babusiaux, C., Haywood, M., & Pelat, D. 2013, A&A, submitted

Havel, M., Guillot, T., Valencia, D., & Crida, A. 2011, A&A, 531, A3+

Hernandez, X., Gilmore, G., & Valls-Gabaud, D. 2000, MNRAS, 317, 831

Holmberg, J., Nordström, B., & Andersen, J. 2009, A&A, 501, 941

Houdek, G. & Gough, D. O. 2007, MNRAS, 375, 861

Iglesias, C. A. & Rogers, F. J. 1996, ApJ, 464, 943

Jørgensen, B. R. & Lindegren, L. 2005, A&A, 436, 127

Kashyap, V. L., Drake, J. J., & Saar, S. H. 2008, ApJ, 687, 1339

Kashyap, V. L., Diake, J. J., & Saar, S. H. 2008, A Kawaler, S. D. 1988, ApJ, 333, 236

Kjeldsen, H. & Bedding, T. R. 1995, A&A, 293, 87

Kjeldsen, H., Bedding, T. R., & Christensen-Dalsgaard, J. 2008, ApJ, 683, L175

Koch, D. G., Borucki, W. J., Basri, G., et al. 2010, ApJ, 713, L79

Kurucz, R. L. 1993, VizieR Online Data Catalog, 6039, 0

Lebreton, Y. 2012, in Astronomical Society of the Pacific Conference Series, Vol. 462, Progress in Solar/Stellar Physics with Helio- and Asteroseismology, ed. H. Shibahashi, M. Takata, & A. E. Lynas-Gray, 469

Lebreton, Y. 2013, in EAS Publications Series, Vol. 63, EAS Publications Series, 123–133

Lebreton, Y. & Goupil, M. J. 2012, A&A, 544, L13

Lebreton, Y., Michel, E., Goupil, M. J., Baglin, A., & Fernandes, J. 1995, in IAU Symposium, Vol. 166, Astronomical and Astrophysical Objectives of Sub-Milliarcsecond Optical Astrometry, ed. E. Hog & P. K. Seidelmann, 135

Lebreton, Y. & Montalbán, J. 2009, in IAU Symposium, Vol. 258, IAU Symposium, ed. E. E. Mamajek, D. R. Soderblom, & R. F. G. Wyse, 419–430

Lebreton, Y., Montalbán, J., Christensen-Dalsgaard, J., Roxburgh, I. W., & Weiss, A. 2008, Ap&SS, 316, 187

Liu, C., Bailer-Jones, C. A. L., Sordo, R., et al. 2012, MNRAS, 426, 2463

Ludwig, H.-G., Freytag, B., & Steffen, M. 1999, A&A, 346, 111

Mamajek, E. E. & Hillenbrand, L. A. 2008, ApJ, 687, 1264

Mamajek, E. E., Meyer, M. R., & Liebert, J. 2002, AJ, 124, 1670

Marques, J. P., Goupil, M. J., Lebreton, Y., et al. 2013, A&A, 549, A74

Mathur, S., Metcalfe, T. S., Woitaszek, M., et al. 2012, ApJ, 749, 152

Mazumdar, A. 2005, A&A, 441, 1079

Metcalfe, T. S., Chaplin, W. J., Appourchaux, T., et al. 2012, ApJ, 748, L10
Michaud, G. & Proffitt, C. R. 1993, in Astronomical Society of the Pacific Conference Series, Vol. 40, IAU Colloq. 137: Inside the Stars, ed. W. W. Weiss & A. Baglin, 246–259

Michel, E., Baglin, A., Auvergne, M., et al. 2008, Science, 322, 558

Miglio, A. & Montalbán, J. 2005, A&A, 441, 615

Morel, P. & Lebreton, Y. 2008, Ap&SS, 316, 61

Morel, P. & Thévenin, F. 2002, A&A, 390, 611

Morel, T., Rainer, M., Poretti, E., Barban, C., & Boumier, P. 2013, A&A, 552, A42

Mosser, B., Michel, E., Belkacem, K., et al. 2013, A&A, 550, A126

Otí Floranes, H., Christensen-Dalsgaard, J., & Thompson, M. J. 2005, MNRAS, 356, 671

Pace, G. 2013, A&A, 551, L8

Peimbert, M., Luridiana, V., & Peimbert, A. 2007, ApJ, 666, 636

Perryman, M. 2011, The Exoplanet Handbook

Pietrinferni, A., Cassisi, S., Salaris, M., & Castelli, F. 2004, ApJ, 612, 168

Pont, F. & Eyer, L. 2004, MNRAS, 351, 487

Press, W. H., Teukolsky, S. A., Vetterling, W. T., & Flannery, B. P. 2002, Numerical recipes in C++: the art of scientific computing

Rauer, H., Catala, C., Aerts, C., et al. 2013, ArXiv e-prints

Table A.1. Specifications of additional optimized models assuming different prescriptions for the modelling.

C /		D 41 1 141	E' 1 1
Set	Case	Particularities	Figure symbol
\boldsymbol{A}	1-Y / 2-Y	Y = 0.25 / 0.27	open red circle
\boldsymbol{A}	$1-\alpha 0.550$	$\alpha_{\rm conv} = 0.550$	open red square
\boldsymbol{A}	$1-\alpha 0.826$	$\alpha_{\rm conv} = 0.826$	open red diamond
\boldsymbol{A}	1-ov0.30	$\alpha_{\rm ov} = 0.30$	open red pentagon
\boldsymbol{A}	1, 2a, 7-vrad		not plotted
\boldsymbol{A}	5-allfreq	-	not plotted
\boldsymbol{A}	6-nocorrel	-	not plotted
\boldsymbol{A}	6-interR	-	not plotted
\boldsymbol{A}	6, 7-ov	optimized overshooting	not plotted
\boldsymbol{A}	6, 7- <i>YM</i>	Y_0 -M degeneracy	open red star
\boldsymbol{A}	7-noSE	no SE corrections	not plotted
\boldsymbol{A}	7-bSE4.9	solar SE corrections	not plotted
\boldsymbol{A}	7-pms	-	not plotted
\boldsymbol{A}	7-rot	rotation	not plotted

Rogers, F. J. & Nayfonov, A. 2002, ApJ, 576, 1064

Roxburgh, I. W. 1992, A&A, 266, 291

Roxburgh, I. W. & Vorontsov, S. V. 1994, MNRAS, 268, 880

Roxburgh, I. W. & Vorontsov, S. V. 2003, A&A, 411, 215

Roxburgh, I. W. & Vorontsov, S. V. 2013, A&A, 560, A2

Scuflaire, R., Montalbán, J., Théado, S., et al. 2008, Ap&SS, 316, 149

Sestito, P. & Randich, S. 2005, A&A, 442, 615

Silva Aguirre, V., Basu, S., Brandão, I. M., et al. 2013, ApJ, 769, 141

Skumanich, A. 1972, ApJ, 171, 565

Soderblom, D. R. 2010, ARA&A, 48, 581

Soriano, M., Vauclair, S., Vauclair, G., & Laymand, M. 2007, A&A, 471, 885

Tassoul, M. 1980, ApJS, 43, 469

Ulrich, R. K. 1986, ApJ, 306, L37

Valle, G., Dell'Omodarme, M., Prada Moroni, P. G., & Degl'Innocenti, S. 2014, A&A, 561, A125

van Leeuwen, F., ed. 2007, Astrophysics and Space Science Library, Vol. 350, Hipparcos, the New Reduction of the Raw Data

VandenBerg, D. A. & Clem, J. L. 2003, AJ, 126, 778

Watson, A. 1998, Science, 279, 981

Zahn, J.-P. 1991, A&A, 252, 179

Appendix A: Models with different input physics or optimization details

A.1. Optimization of set A models with alternate prescriptions

In the following, we present other optimization models, all based on the reference physics of set A (Table 2). These models were optimized following Table 3, but with different approaches or choices of free parameters, as described below and listed in Table A.1. The results of the models are listed in Tables A.2 and A.3.

1. Cases 1 - Y / 2 - Y

As explained in the main text, in cases 1 and 2a, b, and c, the initial helium content Y could not be adjusted because of the lack of observational constraints. Here we investigate the consequence of not deriving Y from the $\Delta Y/\Delta Z=2$ enrichment law (as was done in cases 1 and 2 of Table 3). We sought a solution with the lowest possible initial helium content, never lower than the primordial abundance. These choices have an important impact on the results and are therefore discussed in the main text. We point out that in case A1-Y it was possible to find a solution with a primordial helium abundance. This is because no seismic constraints were used in this case. On the other hand, in cases A2a-Y, b-Y, and c-Y, we had to increase the helium abundance above the primordial one because of the seismic constraints introduced, to find a solution that agreed with both

the seismic and the classical observational constraints (we found that models with low *Y* either have a too low temperature or a too high luminosity).

2. Cases $1-\alpha 0.550$, $1-\alpha 0.826$

In case 1, α_{conv} could not be adjusted because of the lack of observational constraints and, as often seen in papers, the solar value $\alpha_{\text{conv},\odot}$ was used. Here, we investigated the impact of other choices and we sought a solution for acceptable, extreme values of α_{conv} . Numerical 2-D simulations of convection suggest that α_{conv} might differ by a few tenths of dex from the solar value (see e.g. Ludwig et al. 1999). We investigated changes of α_{conv} of 20 per cent around the solar value that correspond to $\alpha_{\text{conv,min}} = 0.550$ and $\alpha_{\text{conv,max}} = 0.826$. These choices have an important impact on the results and are therefore discussed in the main text.

3. Cases 1-ov30

No overshooting was assumed in the reference models of case 1. Here, to estimate its impact, we chose a rather high value, i.e. $\alpha_{ov} = 0.30$. The impact on case 1 results is discussed in the main text.

4. Cases 1, 2, 7-vrad

In these models, the impact of mixing that results from the radiative diffusivity associated with the kinematic radiative viscosity is investigated. Following Morel & Thévenin (2002), we added an extra mixing diffusion coefficient $d_{\rm rad} = D_{\rm R} \times \nu_{\rm rad}$ with $D_{\rm R} = 1$ that limits gravitational settling in the outer stellar layers of stars with thin convective envelopes. As can be seen in Tables A.2 and A.3, the impact is weak and is not discussed further.

5. Case 5-allfreq

In the list of frequencies extracted by Ballot et al. (2011), 31 frequencies were given, of which 28 were flagged as secure. In this model, we considered the 31 values and found that the impact is weak and that the results remain inside the uncertainty range we gave in the main text.

6. Case 6-*YM*, 7-*YM*

For each optimization case, there are a range of initial helium-mass doublets (Y_0, M) that provide seismically equivalent optimized models. We investigated the $Y_0 - M$ degeneracy by searching for optimized models with different values of Y_0 and M. As discussed in the main text, the impact on age is weak but a range of possible masses of HD 52265 is found.

7. Case 6-nocorrel

As explained in the main text, in case 6, we took into account the correlations between the frequency separation ratios and calculated the χ^2 from Eq. 13. In this model the correlations are not considered and the χ^2 is evaluated from Eq. 14. The impact is weak and is not discussed further.

8. Case 6-interr

Roxburgh & Vorontsov (2013) recently claimed that model-fitting by searching for a best fit of observed and model separation ratios at the same radial orders n is incorrect, and that the correct procedure is to compare the model ratios interpolated to the observed frequencies. We followed this recommendation here. The impact is weak and the results remain in the uncertainty range we gave in the main text.

9. Case 7-rot

As explained in the main text, rotation and its effects on the transport of angular momentum and chemicals was treated as in Marques et al. (2013), and we tuned the $K_{\rm w}$ coefficient that enters the treatment of magnetic braking by winds to match the observed rotation period. The impact on age and mass is weak for this rather evolved star. A thorough study

of the effects of rotation on HD 52265 will be presented in a forthcoming paper.

10. Case 7-noSE and case 7-bSE4.9.

As explained in the main text, in case 7, we corrected the individual frequencies for the surface effects with the Kjeldsen et al. (2008) empirical prescription and calibrated the b_{SE} parameter in Eq. 12 to achieve the best match between observed and modelled frequencies. In model 7-bSE4.9, we used the solar value of b_{SE} calibrated by Kjeldsen et al. (2008) and found that the impact on the results is weak. In model 7-noSE, we did not correct frequencies for the surface effects. The impact is strong, in particular on age. This is discussed in the main text.

11. Case 7-pms.

The main models were calculated by starting the computation at the zero-age main sequence. This model was evolved from the pre-main sequence. The impact is weak.

12. Cases 6 and 7-ov.

In the models presented in the main text, overshooting was either neglected (sets A-H, K) or fixed (sets I, J). Since there are enough observational constraints to add overshooting and convective penetration as additional free parameters in cases 6 and 7, we considered this possibility here. We therefore also optimized the values of α_{ov} and ξ_{PC} . As also discussed in the main text, we found that low values of α_{ov} are favoured (range 0.00-0.04) and rather high values of ξ_{PC} (range 0.90-1.25). This latter result, related to the oscillatory behaviour of the frequencies, close to the convective envelope agrees with the conclusions of Lebreton & Goupil (2012).

A.2. Optimization with different input physics

In the following, we present optimization models based on the different choices of input physics listed in Table 2. These models were optimized following Table 3. The results are listed in Tables A.4 and A.5. Discussions are found in the main text.

Table A.2. Same as Table 4, but for different optimization options (see Sect. 3 and Tables A.1 and 3).

Model	Age (Gyr)	M/M_{\odot}	$(Z/X)_0$	Y_0	$lpha_{ m mlt}$	$\alpha_{ m ov}$ / $\xi_{ m PC}$	$b_{ m SE}$	$a_{\rm SE}/r_{\rm SE}$	$\chi^2_{\rm R,classic}/\chi^2_{\rm R,seism}$
A1-Y	1.59 ± 2.17	1.32 ± 0.05	0.0447±0.0051	0.245	0.688	0.00/0.00	_	_	$1.0\ 10^{-19}/\ -$
A1-al0.550	1.03 ± 1.47	1.22 ± 0.03	0.0467 ± 0.0066	0.309	0.550	0.00/0.00	_	_	$1.4 \ 10^{-13}/$ -
A1-al0.826	4.28 ± 0.78	1.15 ± 0.01	0.0471 ± 0.0049	0.310	0.826	0.00/0.00	_	_	$4.1 \ 10^{-5}/$ -
A1-ov 0.3	3.07 ± 1.35	1.18 ± 0.03	0.0487 ± 0.0054	0.312	0.688	0.30/0.00	_	_	$1.8 \ 10^{-17}/$ -
A1-Renu	2.91 ± 1.30	1.18 ± 0.04	0.0481 ± 0.0052	0.311	0.688	0.00/0.00	_	_	$9.7 \ 10^{-6}/$ -
A2a-Renu	2.21 ± 0.87	1.19 ± 0.02	0.0488 ± 0.0051	0.312	0.580 ± 0.096	0.00/0.00	_	_	$1.5 \ 10^{-1} / 5.9 \ 10^{-4}$
A2a-Y	3.46 ± 0.95	1.24 ± 0.01	0.0472 ± 0.0040	0.270	0.682 ± 0.130	0.00/0.00	_	_	$3.3 \ 10^{-1}/1.8 \ 10^{-4}$
A2b-Y	4.27 ± 1.32	1.22 ± 0.03	0.0465 ± 0.0047	0.270	0.744 ± 0.148	0.00/0.00	5.5	-1.3/1.00	$3.6 \ 10^{-1}/1.3 \ 10^{-4}$
A2c-Y	2.63 ± 1.68	1.25 ± 0.04	0.0447 ± 0.0046	0.270	0.604 ± 0.060	0.00/0.00	5.5	-3.3/1.00	$5.3 \ 10^{-1}/2.3 \ 10^{-1}$
A5-allfreq	2.25 ± 0.30	1.27 ± 0.04	0.0461 ± 0.0056	0.265 ± 0.030	0.698 ± 0.081	0.00/0.00	_	_	$8.7 \ 10^{-7} / 3.3 \ 10^{-3}$
A6-YM254	2.45 ± 0.13	1.29 ± 0.01	0.0451 ± 0.0027	0.254 ± 0.008	0.683 ± 0.032	0.00/0.00	_	_	$7.3 \ 10^{-2} / 8.1 \ 10^{-1}$
A6-YM317	2.18 ± 0.11	1.18 ± 0.01	0.0489 ± 0.0025	0.317 ± 0.009	0.591 ± 0.026	0.00/0.00	_	_	$6.7 \ 10^{-2} / 8.9 \ 10^{-1}$
A6-intrr	2.20 ± 0.11	1.17 ± 0.03	0.0494 ± 0.0033	0.324 ± 0.017	0.603 ± 0.031	0.00/0.00	_	_	$1.9 \ 10^{-2} / 8.6 \ 10^{-1}$
A6-nocorrel	2.28 ± 0.21	1.21 ± 0.04	0.0497 ± 0.0051	0.302 ± 0.024	0.595 ± 0.052	0.00/0.00	_	_	$1.8 \ 10^{-1} / 7.2 \ 10^{-1}$
A6-ov	2.32 ± 0.14	1.25 ± 0.01	0.0481 ± 0.0021	0.277 ± 0.006	0.687 ± 0.027	0.04/0.90	_	_	$2.0\ 10^{-1}/7.8\ 10^{-1}$
A7-bSE4.9	2.18 ± 0.03	1.27 ± 0.00	0.0487 ± 0.0006	0.274 ± 0.001	0.601 ± 0.004	0.00/0.00	4.9	-4.1/1.00	$5.3 \ 10^{-1}/1.8 \ 10^{0}$
A7-Renu	2.18 ± 0.02	1.27 ± 0.00	0.0489 ± 0.0007	0.274 ± 0.001	0.599 ± 0.004	0.00/0.00	4.5	-4.7/1.00	$4.9 \ 10^{-1}/1.7 \ 10^{0}$
A7-YM-noSE	2.98 ± 0.03	1.24 ± 0.00	0.0628 ± 0.0007	0.306 ± 0.001	0.725 ± 0.005	0.00/0.00	_	_	$3.3 \ 10^{0} / 6.8 \ 10^{0}$
A7-ov	1.93 ± 0.01	1.23 ± 0.00	0.0481 ± 0.0007	0.291 ± 0.001	0.564 ± 0.003	0.00/1.25	3.6	-7.7/1.00	$7.8 \ 10^{-1}/2.2 \ 10^{0}$
A7- YM -ov	2.15 ± 0.03	1.23 ± 0.00	0.0485 ± 0.0007	0.289 ± 0.001	0.581 ± 0.003	0.00/0.99	4.1	-5.9/1.00	$5.7 \ 10^{-1}/1.8 \ 10^{0}$
A7-noSE	3.14 ± 0.03	1.30 ± 0.00	0.0690 ± 0.0008	0.276 ± 0.001	0.731 ± 0.005	0.00/0.00	_	_	$4.7 \ 10^{0} / 4.0 \ 10^{0}$
A7-pms	2.18 ± 0.02	1.27 ± 0.00	0.0486 ± 0.0006	0.274 ± 0.001	0.601 ± 0.004	0.00/0.00	3.8	-6.2/1.00	$5.2 \ 10^{-1}/1.7 \ 10^{0}$
A7-YM244	2.14 ± 0.02	1.32 ± 0.00	0.0460 ± 0.0008	0.244 ± 0.001	0.588 ± 0.004	0.00/0.00	4.5	-4.4/1.00	$7.7 \ 10^{-1}/1.6 \ 10^{0}$
A7-YM260	2.18 ± 0.03	1.28 ± 0.00	0.0467 ± 0.0006	0.260 ± 0.001	0.583 ± 0.004	0.00/0.00	3.7	-6.4/1.00	$5.9 \ 10^{-1}/1.6 \ 10^{0}$
A7-YM300	2.14 ± 0.01	1.21 ± 0.00	0.0478 ± 0.0006	0.300 ± 0.001	0.585 ± 0.004	0.00/0.00	3.8	-7.3/1.00	$1.7 \ 10^{-1}/1.8 \ 10^{0}$
A7-YM310	2.16 ± 0.02	1.20 ± 0.00	0.0484 ± 0.0004	0.310 ± 0.001	0.584 ± 0.004	0.00/0.00	3.5	-8.2/1.00	$1.2 \ 10^{-1}/1.9 \ 10^{0}$
A7-YM320	2.17 ± 0.02	1.18 ± 0.00	0.0501 ± 0.0004	0.320 ± 0.001	0.585 ± 0.004	0.00/0.00	3.5	-8.3/1.00	$1.3 \ 10^{-1}/2.0 \ 10^{0}$
A7-YM335	2.15 ± 0.02	1.15 ± 0.00	0.0491 ± 0.0003	0.335 ± 0.001	0.585 ± 0.004	0.00/0.00	3.5	-2.0/1.00	$2.6\ 10^{-2}/2.1\ 10^{0}$
A7-rot	2.19 ± 0.03	1.27 ± 0.00	0.0488 ± 0.0004	0.275 ± 0.001	0.595 ± 0.004	0.00/0.00	5.5	-3.3/1.00	$1.3\ 10^{0}/2.6\ 10^{0}$

Table A.3. Same as Table 5, but for different optimization options (see Sect. 3 and Tables A.1 and 3)

Model	$T_{ m eff}$	L	[Fe/H]	$\log g$	R	$\langle \Delta \nu \rangle$	$\nu_{ m max}$	$\langle r_{02} \rangle$	$\langle rr_{01/10} \rangle$	X_C	$\frac{\Delta Y}{\Delta Z}$	$M_{\rm cc}$	R_{zc}	$M_{\rm p} \sin i$
	[K]	$[L_{\odot}]$	[dex]	[dex]	$[R_{\odot}]$	$[\mu Hz]$	$[\mu Hz]$	_	_	_	ΔZ	$[M_{\star}]$	$[R_{\star}]$	$[M]_{ m Jupiter}]$
A1-Y	6116.	2.053	0.22	4.35	1.28	107.45	2393.	0.091	0.033	0.49	0.0	0.002	0.788	1.27±0.04
A1-al0.550	6116.	2.053	0.22	4.31	1.28	101.88	2210.	0.097	0.035	0.51	2.0	0.016	0.836	1.20 ± 0.04
A1-al0.826	6116.	2.053	0.22	4.29	1.28	101.09	2081.	0.053	0.030	0.16	2.0	0.047	0.713	1.15 ± 0.03
A1-ov 0.3	6116.	2.053	0.22	4.30	1.28	101.27	2131.	0.072	0.011	0.43	2.0	0.140	0.769	1.17 ± 0.04
A1-Renu	6116.	2.054	0.22	4.29	1.28	101.29	2125.	0.074	0.033	0.28	2.0	0.029	0.769	1.17 ± 0.04
A2a-Renu	6046.	2.062	0.22	4.28	1.31	98.13	2064.	0.083	0.035	0.35	2.0	0.023	0.806	1.18 ± 0.03
A2a-Y	6012.	2.069	0.21	4.28	1.33	98.13	2096.	0.070	0.033	0.27	0.7	0.024	0.759	1.21 ± 0.03
A2b-Y	6008.	2.070	0.21	4.28	1.33	98.13	2063.	0.060	0.032	0.21	0.7	0.036	0.731	1.20 ± 0.04
A2c-Y	6001.	2.060	0.19	4.29	1.33	98.26	2106.	0.080	0.034	0.33	0.7	0.010	0.791	1.22 ± 0.04
A5-allfreq	6116.	2.053	0.22	4.33	1.28	105.37	2299.	0.083	0.033	0.39	0.5	0.007	0.778	1.23 ± 0.04
A6-YM254	6074.	2.058	0.21	4.32	1.30	103.67	2263.	0.081	0.032	0.37	0.2	0.005	0.777	1.24 ± 0.03
A6-YM317	6068.	2.048	0.22	4.28	1.30	98.69	2087.	0.084	0.034	0.35	2.2	0.022	0.804	1.18 ± 0.03
A6-intrr	6094.	2.060	0.22	4.29	1.29	99.07	2085.	0.083	0.034	0.34	2.4	0.026	0.802	1.17 ± 0.04
A6-nocorrel	6037.	2.054	0.23	4.28	1.31	98.29	2092.	0.083	0.034	0.35	1.7	0.020	0.799	1.19 ± 0.04
A6-ov	6094.	2.039	0.26	4.32	1.28	104.20	2252.	0.082	0.032	0.39	0.9	0.017	0.729	1.22 ± 0.03
A7-bSE4.9	6019.	2.101	0.23	4.29	1.34	98.29	2123.	0.084	0.034	0.39	0.8	0.014	0.800	1.23 ± 0.03
A7-Renu	6013.	2.092	0.23	4.29	1.34	98.29	2125.	0.084	0.034	0.39	0.8	0.013	0.800	1.23 ± 0.03
A7-YM-noSE	6069.	2.156	0.34	4.28	1.33	98.30	2076.	0.070	0.030	0.29	1.4	0.046	0.754	1.21 ± 0.03
A7-ov	5989.	2.012	0.25	4.29	1.32	98.28	2112.	0.087	0.034	0.41	1.3	0.012	0.753	1.21 ± 0.03
A7-YM-ov	5997.	2.030	0.25	4.29	1.32	98.28	2107.	0.085	0.034	0.38	1.3	0.013	0.756	1.21 ± 0.03
A7-noSE	5983.	2.114	0.39	4.29	1.36	98.33	2122.	0.070	0.030	0.31	0.6	0.041	0.745	1.26 ± 0.03
A7-pms	6021.	2.101	0.23	4.29	1.33	98.29	2125.	0.084	0.034	0.39	0.8	0.013	0.800	1.23 ± 0.03
A7-YM244	5958.	2.073	0.21	4.30	1.35	98.29	2160.	0.086	0.033	0.42	0.0	0.003	0.800	1.27 ± 0.03
A7-YM260	5971.	2.048	0.21	4.29	1.34	98.28	2141.	0.085	0.033	0.40	0.4	0.006	0.801	1.24 ± 0.03
A7-YM300	6047.	2.067	0.21	4.29	1.31	98.28	2096.	0.084	0.034	0.37	1.7	0.017	0.806	1.20 ± 0.03
A7-YM310	6047.	2.046	0.21	4.28	1.31	98.28	2087.	0.084	0.034	0.36	2.0	0.019	0.805	1.19 ± 0.03
A7-YM320	6055.	2.038	0.23	4.28	1.30	98.28	2077.	0.084	0.034	0.35	2.3	0.023	0.804	1.17 ± 0.03
A7-YM335	6090.	2.045	0.21	4.28	1.29	98.29	2058.	0.083	0.035	0.34	2.9	0.027	0.807	1.15 ± 0.03
A7-rot	6034.	2.124	0.28	4.29	1.34	98.32	2121.	0.085	0.034	0.40	0.8	0.014	0.806	1.23±0.03

Table A.4. Same as Table 4, but for different input physics of the models (see Sect. 3 and Tables 2 and 3).

Model	Age (Gyr)	M/M_{\odot}	$(Z/X)_0$	Y_0	ο,	$\alpha_{ m ov} / \xi_{ m PC}$	$b_{ m SE}$	gan/ran	1,2 /1,2
B1	2.62 ± 1.22	1.18 ± 0.03	0.0483 ± 0.0053	0.311	$\frac{\alpha_{\rm mlt}}{1.762}$	$\frac{\alpha_{\text{ov}} / \xi_{\text{PC}}}{0.00/0.00}$	–	$a_{\rm SE}/r_{\rm SE}$	$\chi^2_{\text{R,classic}}/\chi^2_{\text{R,seism}}$ $4.6 \ 10^{-7}/$
<i>B</i> 1 <i>B</i> 2a	1.80 ± 0.85	1.18 ± 0.03 1.20 ± 0.02	0.0493±0.0054	0.311	1.702 1.473±0.222	0.00/0.00		_	$1.8 \ 10^{-1}/6.2 \ 10^{-4}$
<i>B</i> 2a <i>B</i> 2b	1.80 ± 0.83 2.18 ± 0.78	1.20 ± 0.02 1.19 ± 0.02	0.0491±0.0051	0.312	1.473 ± 0.222 1.562 ± 0.252	0.00/0.00	- 5.5	-4.8/1.00	$1.8 \ 10^{-1}/0.2 \ 10^{-1}$ $1.2 \ 10^{-1}/1.9 \ 10^{-4}$
B20 B2c	2.18 ± 0.78 2.18 ± 0.55	1.19 ± 0.02 1.19 ± 0.01	0.0491 ± 0.0051 0.0491 ± 0.0051	0.312	1.562 ± 0.232 1.562 ± 0.242	0.00/0.00	5.5	-4.8/1.00	$2.2 \ 10^{-1} / 7.9 \ 10^{-6}$
			0.0491 ± 0.0031 0.0489 ± 0.0053	0.312 0.299±0.019			J.J –		$2.6 \ 10^{-1}/1.7 \ 10^{-2}$
B3	1.91 ± 1.12	1.23 ± 0.01			1.500±0.241	0.00/0.00		- 5 4/1 00	
B4	2.06 ± 0.24	1.12 ± 0.02	0.0511±0.0047	0.355±0.017	1.549±0.096	0.00/0.00	5.5	-5.4/1.00	$3.2 \ 10^{-5} / 7.0 \ 10^{-7}$
B5	2.17 ± 0.32	1.24 ± 0.05	0.0467 ± 0.0061	0.281±0.040	1.769±0.229	0.00/0.00	_	_	$7.4 \ 10^{-7} / 4.0 \ 10^{-3}$
B6	2.26 ± 0.12	1.24 ± 0.02	0.0470 ± 0.0020	0.283±0.009	1.571±0.065	0.00/0.00	_ 2.5	- 0.2/1.00	$3.0 \ 10^{-1} / 8.3 \ 10^{-1}$
<i>B</i> 7	2.49 ± 0.02	1.23 ± 0.00	0.0494±0.0005	0.289±0.001	1.615±0.009	0.00/0.00	3.5	-8.3/1.00	$3.2 \ 10^{-1}/1.8 \ 10^{0}$
C1	2.98± 1.33	1.18± 0.03	0.0358 ± 0.0038	0.296	0.688	0.00/0.00	_	_	1.1 10 ⁻⁸ / -
C2a	3.22 ± 1.08	1.18 ± 0.02	0.0363±0.0037	0.297	0.656±0.111	0.00/0.00	_	-	$1.0\ 10^{-1}/9.8\ 10^{-5}$
C2b	1.64 ± 0.67	1.22 ± 0.02	0.0363±0.0053	0.297	0.544 ± 0.074	0.00/0.00	5.5	-5.0/1.00	$1.4\ 10^{-1}/6.2\ 10^{-4}$
C2c	1.64 ± 0.66	1.22 ± 0.02	0.0363 ± 0.0047	0.297	0.544 ± 0.083	0.00/0.00	5.5	-5.0/1.00	$1.5 \ 10^{-1}/3.6 \ 10^{-4}$
C3	2.56 ± 1.18	1.23 ± 0.03	0.0361±0.0038	0.280±0.023	0.601 ± 0.092	0.00/0.00	_	-	$2.7 \ 10^{-1} / 8.8 \ 10^{-3}$
C4	2.22 ± 0.27	1.14 ± 0.02	0.0380±0.0032	0.336±0.016	0.587 ± 0.048	0.00/0.00	5.5	-4.9/1.00	$1.9 \ 10^{-3}/2.5 \ 10^{-6}$
C5	2.28 ± 0.31	1.24 ± 0.03	0.0346±0.0038	0.272±0.019	0.670 ± 0.075	0.00/0.00	_	_	$8.1 \ 10^{-5}/2.5 \ 10^{-3}$
<i>C</i> 6	2.44 ± 0.13	1.24 ± 0.02	0.0363±0.0016	0.275 ± 0.011	0.606 ± 0.025	0.00/0.00	_		$2.4 \ 10^{-1} / 8.3 \ 10^{-1}$
<i>C</i> 7	2.43 ± 0.03	1.24 ± 0.00	0.0358±0.0004	0.272±0.001	0.598±0.004	0.00/0.00	3.5	-7.6/1.00	$2.9 \ 10^{-1}/1.5 \ 10^{0}$
D1	2.72 ± 1.08	1.18 ± 0.02	0.0478 ± 0.0055	0.310	0.688	0.00/0.00	_	_	8.2 10 ⁻⁷ / -
D2a	2.66 ± 0.90	1.19 ± 0.02	0.0485 ± 0.0051	0.311	0.630 ± 0.104	0.00/0.00	_	_	$1.3 \ 10^{-1}/2.1 \ 10^{-6}$
D2b	1.72 ± 0.87	1.21 ± 0.02	0.0492 ± 0.0050	0.312	0.560 ± 0.114	0.00/0.00	5.5	-4.4/1.00	$1.5 \ 10^{-1} / 1.4 \ 10^{-3}$
D2c	2.09 ± 1.02	1.20 ± 0.02	0.0488 ± 0.0052	0.312	0.585 ± 0.093	0.00/0.00	5.5	-3.9/1.00	$2.4 \ 10^{-1} / 5.0 \ 10^{-4}$
D3	2.01 ± 1.08	1.23 ± 0.03	0.0487 ± 0.0068	0.300 ± 0.026	0.574 ± 0.083	0.00/0.00	_	_	$2.6 \ 10^{-1} / 1.6 \ 10^{-2}$
D4	2.03 ± 0.24	1.14 ± 0.02	0.0501 ± 0.0049	0.348 ± 0.017	0.583 ± 0.040	0.00/0.00	5.5	-4.4/1.00	$5.6\ 10^{-3}/6.2\ 10^{-6}$
D5	2.08 ± 0.25	1.18 ± 0.06	0.0484 ± 0.0050	0.323 ± 0.045	0.620 ± 0.159	0.00/0.00	_	_	$4.2\ 10^{-5}/7.6\ 10^{-3}$
D6	2.28 ± 0.12	1.23 ± 0.02	0.0452 ± 0.0017	0.287 ± 0.008	0.588 ± 0.022	0.00/0.00	_	_	$3.9 \ 10^{-1} / 8.1 \ 10^{-1}$
D7	2.05 ± 0.02	1.23 ± 0.00	0.0485 ± 0.0007	0.297 ± 0.001	0.594 ± 0.004	0.00/0.00	4.3	-5.3/1.00	$3.0\ 10^{-1}/2.0\ 10^{0}$
<i>E</i> 1	4.50± 1.70	1.13 ± 0.06	0.0405±0.0046	0.302	0.688	0.00/0.00	_	_	$5.6\ 10^{-3}/$ -
<i>E</i> 2a	1.40 ± 0.99	1.21 ± 0.02	0.0404 ± 0.0046	0.302	0.466 ± 0.082	0.00/0.00	_	_	$1.9 \ 10^{-1} / 3.9 \ 10^{-4}$
E2b	1.26 ± 0.89	1.21 ± 0.02	0.0405 ± 0.0046	0.302	0.479 ± 0.085	0.00/0.00	5.5	-5.7/1.00	$8.8 \ 10^{-2} / 6.1 \ 10^{-4}$
E2c	1.90 ± 1.06	1.19 ± 0.02	0.0406 ± 0.0046	0.302	0.516 ± 0.072	0.00/0.00	5.5	-5.1/1.00	$1.8 \ 10^{-1}/2.2 \ 10^{-3}$
<i>E</i> 3	1.61 ± 1.44	1.22 ± 0.03	0.0406 ± 0.0046	0.290 ± 0.025	0.488 ± 0.093	0.00/0.00	_	_	$2.6 \ 10^{-1}/2.5 \ 10^{-2}$
E4	1.79 ± 0.28	1.22 ± 0.02	0.0416 ± 0.0047	0.291±0.018	0.515 ± 0.034	0.00/0.00	5.5	-4.9/1.00	$1.7 \ 10^{-1}/2.2 \ 10^{0}$
E5	2.33 ± 0.40	1.24 ± 0.04	0.0406 ± 0.0047	0.269 ± 0.023	0.633 ± 0.093	0.00/0.00	_	_	$2.0 \ 10^{-5} / 3.3 \ 10^{-3}$
<i>E</i> 6	2.46 ± 0.08	1.19 ± 0.01	0.0462 ± 0.0018	0.309 ± 0.004	0.591 ± 0.027	0.00/0.00	_	_	$5.8 \ 10^{-1} / 9.4 \ 10^{-1}$
<i>E</i> 7	1.70 ± 0.01	1.23 ± 0.00	0.0417±0.0007	0.287 ± 0.001	0.506 ± 0.003	0.00/0.00	3.8	-9.0/1.00	$4.3 \ 10^{-1} / 7.1 \ 10^{0}$
<i>F</i> 1	2.85 ± 1.18	1.18 ± 0.02	0.0482±0.0052	0.311	2.000	0.00/0.00	_		$1.5 \ 10^{-6}/$ -
F2a	3.52 ± 0.96	1.17 ± 0.01	0.0482 ± 0.0052	0.311	2.057 ± 0.472	0.00/0.00	_	_	$6.7 \ 10^{-2} / 1.2 \ 10^{-2}$
F2b	2.38 ± 0.93	1.19 ± 0.02	0.0491±0.0050	0.312	1.732±0.342	0.00/0.00	5.5	-4.1/1.00	$1.2 \ 10^{-1}/6.7 \ 10^{-2}$
F2c	3.33 ± 0.91	1.17 ± 0.02	0.0488 ± 0.0050	0.312	2.008±0.331	0.00/0.00	5.5	-2.7/1.00	$2.0\ 10^{-1}/1.1\ 10^{-5}$
F3	1.06± 1.13	1.23 ± 0.02	0.0487±0.0079	0.311±0.027	1.397 ± 0.270	0.00/0.00	_	_	$2.6 \ 10^{-1}/1.5 \ 10^{-2}$
F4	2.08 ± 0.25	1.13 ± 0.02	0.0508 ± 0.0043	0.350 ± 0.016	1.674±0.142	0.00/0.00	5.5	-4.9/1.00	$1.9 \ 10^{-3} / 8.5 \ 10^{-6}$
F5	2.17 ± 0.31	1.25 ± 0.05	0.0466±0.0061	0.281±0.035	1.955±0.244	0.00/0.00	_	-	$1.1 \ 10^{-6} / 4.0 \ 10^{-3}$
F6	2.29 ± 0.13	1.25 ± 0.03 1.25 ± 0.02	0.0456 ± 0.0017	0.277 ± 0.007	1.690±0.090	0.00/0.00	_	_	$4.1 \ 10^{-1} / 8.2 \ 10^{-1}$
F7	2.67 ± 0.02	1.18 ± 0.00	0.0477 ± 0.0004	0.310 ± 0.001	1.848±0.013	0.00/0.00	3.5	-7.2/1.00	$2.7 \ 10^{-1}/2.2 \ 10^{0}$
G1	2.94± 1.33	1.18 ± 0.03	0.0488 ± 0.0057	0.312	0.688	0.00/0.00	-	-	$\frac{2.7 \cdot 10^{-7}/2.2 \cdot 10^{-7}}{4.0 \cdot 10^{-7}/-}$
G2a	1.39 ± 0.84	1.10 ± 0.03 1.22 ± 0.02	0.0503±0.0088	0.312	0.514±0.073	0.00/0.00	_	_	$2.3 \ 10^{-1}/1.5 \ 10^{-3}$
G2b	1.37 ± 0.64 1.21 ± 0.59	1.22 ± 0.02 1.22 ± 0.02	0.0303 ± 0.0088 0.0494 ± 0.0186	0.313	0.514 ± 0.073 0.515 ± 0.050	0.00/0.00	5.5	-5.2/1.00	$1.4 \ 10^{-1}/4.3 \ 10^{-4}$
G2c	2.51 ± 0.99	1.19 ± 0.02	0.0494 ± 0.0180 0.0499 ± 0.0051	0.312	0.608 ± 0.093	0.00/0.00	5.5	-3.7/1.00	$2.0 \ 10^{-1}/1.7 \ 10^{-3}$
G3	1.12 ± 1.15	1.19 ± 0.02 1.22 ± 0.00	0.0499 ± 0.0031 0.0502 ± 0.0239	0.313±0.035	0.493±0.115	0.00/0.00	_	-3.7/1.00	$2.6 \ 10^{-1}/2.0 \ 10^{-2}$
G4	2.09 ± 0.25	1.13 ± 0.02	0.0508±0.0056	0.348 ± 0.021	0.581 ± 0.028	0.00/0.00	3.8	-8.5/1.00	$7.5 \ 10^{-3}/6.4 \ 10^{-1}$
G5	2.07 ± 0.23 2.17 ± 0.31	1.13 ± 0.02 1.25 ± 0.04	0.0471±0.0059	0.281 ± 0.033	0.667 ± 0.028	0.00/0.00	<i>J</i> .0	-0.5/1.00	$3.9 \ 10^{-7} / 4.2 \ 10^{-3}$
G6	2.17 ± 0.31 2.33 ± 0.12	1.23 ± 0.04 1.26 ± 0.02	0.0471 ± 0.0039 0.0477 ± 0.0023	0.281 ± 0.033 0.274 ± 0.010	0.597 ± 0.082	0.00/0.00	_	_	$3.6 \ 10^{-1}/8.0 \ 10^{-1}$
G7	2.33 ± 0.12 2.16 ± 0.02	1.20 ± 0.02 1.27 ± 0.00	0.0477 ± 0.0023 0.0474 ± 0.0007	0.274 ± 0.010 0.271 ± 0.001	0.586±0.004	0.00/0.00	4.0	-5.7/1.00	$4.2 \ 10^{-1}/1.7 \ 10^{0}$
H1	2.10 ± 0.02 2.90 ± 1.77	1.27 ± 0.00 1.18 ± 0.04	0.0474±0.0007 0.0483±0.0063	0.271±0.001	0.580±0.004 0.688	0.00/0.00	-	-3.7/1.00	$\frac{4.2 \text{ 10}^{-1.7 \text{ 10}}}{7.4 \text{ 10}^{-8}/-}$
H1 H2a	1.63 ± 0.86	1.18 ± 0.04 1.21 ± 0.02	0.0483 ± 0.0003 0.0494 ± 0.0055	0.311	0.534 ± 0.087	0.00/0.00	_	_	$2.0 \ 10^{-1} / 4.7 \ 10^{-4}$
H2a H2b	1.63 ± 0.86 1.87 ± 0.78	1.21 ± 0.02 1.20 ± 0.02	0.0494 ± 0.0055 0.0491 ± 0.0052	0.312		0.00/0.00	5.5	-4.5/1.00	$1.2 \ 10^{-1} / 5.0 \ 10^{-4}$
				0.312	0.563 ± 0.096				$2.2 \ 10^{-1} / 9.4 \ 10^{-4}$
H2с нз	2.12 ± 0.98	1.20 ± 0.02	0.0493 ± 0.0052		0.582 ± 0.087	0.00/0.00	5.5	-4.1/1.00	$2.6 \ 10^{-1}/1.7 \ 10^{-2}$
H3	1.80 ± 1.14	1.23 ± 0.01	0.0490±0.0053	0.301 ± 0.020	0.550 ± 0.097	0.00/0.00	- 5.5	- 4.7/1.00	$1.5 \ 10^{-3} / 1.6 \ 10^{-6}$
H4 115	2.09 ± 0.25	1.13 ± 0.02	0.0509 ± 0.0045	0.349 ± 0.016	0.581 ± 0.040	0.00/0.00	5.5	-4.7/1.00	
H5	2.17 ± 0.34	1.25 ± 0.06	0.0467 ± 0.0066	0.280 ± 0.048	0.671 ± 0.110	0.00/0.00	_	_	$1.4 \ 10^{-6} / 4.0 \ 10^{-3}$
H6	2.29 ± 0.12	1.27 ± 0.02	0.0481 ± 0.0023	0.273±0.010	0.605 ± 0.021	0.00/0.00	-	- 5 0/1 00	$4.1\ 10^{-1}/8.1\ 10^{-1}$
H7	2.19 ± 0.02	1.27 ± 0.00	0.0486±0.0007	0.273±0.001	0.598±0.004	0.00/0.00	4.3	-5.0/1.00	$\frac{4.6 \ 10^{-1}/1.7 \ 10^{0}}{2.2 \ 10^{-12}}$
<i>I</i> 1	2.95 ± 1.23	1.18 ± 0.03	0.0485 ± 0.0053	0.311	0.688	0.15/0.00	_	_	$3.2 \ 10^{-12}/$ -

Table A.4. continued.

Model	Age (Gyr)	M/M_{\odot}	$(Z/X)_0$	Y_0	$lpha_{ m mlt}$	$\alpha_{ m ov}$ / $\xi_{ m PC}$	$b_{ m SE}$	$a_{\rm SE}/r_{\rm SE}$	$\chi^2_{\rm R,classic}/\chi^2_{\rm R,seism}$
<i>I</i> 2a	2.49 ± 0.85	1.19 ± 0.02	0.0494 ± 0.0051	0.312	0.602±0.096	0.15/0.00	_	_	$1.3 \ 10^{-1} / 5.7 \ 10^{-4}$
<i>I</i> 2b	1.85 ± 0.77	1.20 ± 0.02	0.0492 ± 0.0055	0.312	0.560 ± 0.094	0.15/0.00	5.5	-4.5/1.00	$1.3 \ 10^{-1} / 4.8 \ 10^{-4}$
I2c	2.07 ± 0.97	1.20 ± 0.02	0.0494 ± 0.0058	0.312	0.576 ± 0.084	0.15/0.00	5.5	-4.2/1.00	$2.4 \ 10^{-1} / 9.9 \ 10^{-4}$
<i>I</i> 3	1.99 ± 1.33	1.23 ± 0.03	0.0490 ± 0.0053	0.299 ± 0.023	0.564 ± 0.092	0.15/0.00	_	_	$2.6 \ 10^{-1}/1.5 \ 10^{-2}$
<i>I</i> 4	2.08 ± 0.24	1.18 ± 0.02	0.0497 ± 0.0049	0.320 ± 0.016	0.577 ± 0.038	0.15/0.00	5.5	-4.3/1.00	$8.0\ 10^{-2}/9.3\ 10^{-4}$
<i>I</i> 5	2.03 ± 0.37	1.39 ± 0.02	0.0425 ± 0.0047	0.204 ± 0.004	0.703 ± 0.121	0.15/0.00	_	_	$2.2 \ 10^{-1} / 8.5 \ 10^{-1}$
<i>I</i> 6	2.22 ± 0.11	1.20 ± 0.01	0.0482 ± 0.0024	0.303 ± 0.006	0.591 ± 0.029	0.15/0.00	_	_	$2.9 \ 10^{-1}/4.5 \ 10^{0}$
<i>I</i> 7	2.17 ± 0.02	1.27 ± 0.00	0.0488 ± 0.0007	0.274 ± 0.001	0.596 ± 0.004	0.15/0.00	4.4	-4.8/1.00	$4.7 \ 10^{-1}/3.0 \ 10^{0}$
J1	3.02± 1.39	1.18 ± 0.03	0.0487±0.0056	0.311	0.688	1.80/0.00	_	_	$7.0 \ 10^{-6}/$ -
J2a	1.66 ± 0.85	1.21 ± 0.02	0.0497 ± 0.0066	0.313	0.532 ± 0.082	1.80/0.00	_	_	$2.1 \ 10^{-1} / 5.8 \ 10^{-4}$
J2b	1.73 ± 0.74	1.21 ± 0.02	0.0492 ± 0.0061	0.312	0.548 ± 0.089	1.80/0.00	5.5	-4.8/1.00	$1.4 \ 10^{-1} / 4.1 \ 10^{-4}$
J2c	2.06 ± 0.91	1.20 ± 0.02	0.0495 ± 0.0070	0.312	0.571 ± 0.078	1.80/0.00	5.5	-4.4/1.00	$2.5 \ 10^{-1}/4.7 \ 10^{-4}$
J3	1.99 ± 0.95	1.23 ± 0.01	0.0493 ± 0.0057	0.301 ± 0.019	0.560 ± 0.099	1.80/0.00	_	_	$2.6 \ 10^{-1}/1.4 \ 10^{-2}$
J4	2.02 ± 0.22	1.13 ± 0.02	0.0517 ± 0.0048	0.356 ± 0.015	0.569 ± 0.041	1.80/0.00	5.5	-5.1/1.00	$5.5 \ 10^{-7} / 1.2 \ 10^{-5}$
J5	0.80 ± 0.24	1.43 ± 0.07	0.0442 ± 0.0052	0.200 ± 0.048	0.890 ± 0.282	1.80/0.00	_	_	$5.3 \ 10^{-1}/6.8 \ 10^{0}$
J6	1.73 ± 0.09	1.21 ± 0.02	0.0528 ± 0.0022	0.315 ± 0.008	0.585 ± 0.020	1.80/0.00	_	_	$2.4 \ 10^{-1} / 8.3 \ 10^{0}$
J7	2.02 ± 0.01	1.23 ± 0.00	0.0489 ± 0.0008	0.296 ± 0.001	0.566 ± 0.003	1.80/0.00	4.2	-6.5/1.00	$3.1 \ 10^{-1} / 5.5 \ 10^{0}$
<i>K</i> 1	2.87 ± 1.22	1.17 ± 0.03	0.0448±0.0049	0.307	0.688	0.00/1.30	_	_	$1.2 \ 10^{-5}/$ -
<i>K</i> 2a	2.43 ± 0.86	1.18 ± 0.02	0.0452 ± 0.0049	0.307	0.600 ± 0.095	0.00/1.30	_	_	$1.5 \ 10^{-1}/1.1 \ 10^{-3}$
<i>K</i> 2b	1.70 ± 0.74	1.20 ± 0.02	0.0450 ± 0.0052	0.307	0.547 ± 0.093	0.00/1.30	5.5	-4.7/1.00	$1.3 \ 10^{-1} / 4.8 \ 10^{-4}$
<i>K</i> 2c	2.32 ± 0.96	1.19 ± 0.02	0.0450 ± 0.0049	0.307	0.592 ± 0.090	0.00/1.30	5.0	-4.7/1.00	$2.4 \ 10^{-1} / 5.4 \ 10^{-4}$
<i>K</i> 3	2.11 ± 1.06	1.22 ± 0.02	0.0450 ± 0.0049	0.293 ± 0.019	0.575 ± 0.109	0.00/1.30	_	_	$2.7 \ 10^{-1}/1.2 \ 10^{-2}$
<i>K</i> 4	2.12 ± 0.24	1.12 ± 0.02	0.0464 ± 0.0044	0.347 ± 0.016	0.577 ± 0.044	0.00/1.30	5.5	-4.7/1.00	$1.3 \ 10^{-3} / 1.6 \ 10^{-6}$
<i>K</i> 5	2.18 ± 0.31	1.25 ± 0.03	0.0438 ± 0.0050	0.275 ± 0.023	0.682 ± 0.075	0.00/1.30	_	_	$3.2 \ 10^{-6} / 1.6 \ 10^{-3}$
<i>K</i> 6	1.92 ± 0.07	1.24 ± 0.01	0.0489 ± 0.0014	0.292 ± 0.003	0.603 ± 0.012	0.00/1.30	_	_	$1.4 \ 10^{0} / 8.9 \ 10^{-1}$
<i>K</i> 7	2.14 ± 0.01	1.22 ± 0.00	0.0494 ± 0.0006	0.301 ± 0.001	0.592 ± 0.003	0.00/1.30	3.8	-6.5/1.00	$6.1\ 10^{-1}/2.7\ 10^{0}$

Table A.5. Same as Table 5, but for different input physics of the models (see Sect. 3 and Tables 2 and 3).

Model	$T_{ m eff}$	L	[Fe/H]	$\log g$	R	$\langle \Delta \nu \rangle$	$\nu_{ m max}$	$\langle r_{02} \rangle$	$\langle rr_{01/10} \rangle$	X_C	$\frac{\Delta Y}{\Delta Z}$	$R_{\rm cc}$	$R_{\rm zc}$	$M_{\rm p} \sin i$
<i>B</i> 1	[K] 6116.	$[L_{\odot}]$ 2.053	[dex] 0.22	[dex] 4.30	$[R_{\odot}]$ 1.28	[μHz] 101.45	[μHz] 2138.	0.078	0.034	0.31	2.0	$\frac{[R_{\star}]}{0.027}$	$[R_{\star}]$ 0.779	$\frac{[M_{\text{Jupiter}}]}{1.18\pm0.03}$
B1 B2a	6038.	2.053	0.22	4.30	1.28	98.13	2138. 2072.	0.078	0.034	0.31	2.0	0.027	0.779	1.18±0.03 1.19±0.03
<i>B</i> 2b	6053.	2.063	0.22	4.28	1.31	98.13	2073.	0.084	0.033	0.36	2.0	0.023	0.806	1.19 ± 0.03 1.18 ± 0.03
B2c	6053.	2.063	0.22	4.28	1.31	98.21	2073.	0.084	0.034	0.36	2.0	0.023	0.806	1.18 ± 0.03
<i>B</i> 3	6022.	2.066	0.22	4.28	1.32	98.14	2087.	0.087	0.034	0.40	1.6	0.017	0.815	1.20 ± 0.03
B4	6116.	2.054	0.22	4.27	1.28	98.14	2028.	0.084	0.035	0.33	3.4	0.034	0.812	1.14±0.03
B5	6116.	2.053	0.22	4.32	1.28	104.12	2250.	0.084	0.033	0.38	1.1	0.011	0.786	1.22±0.05
B6 B7	6016. 6012.	2.062 2.046	0.21 0.23	4.29 4.29	1.32 1.32	98.28 98.28	2109. 2099.	0.084 0.081	0.034 0.034	0.37 0.34	1.1 1.3	0.013 0.019	0.802 0.792	1.21±0.03 1.21±0.03
C1	6116.	2.040	0.23	4.29	1.32	101.39	2139.	0.104	0.034	0.34	2.0	0.019	0.792	1.21±0.03 1.18±0.04
C2a	6057.	2.062	0.22	4.28	1.31	98.13	2054.	0.104	0.034	0.24	2.0	0.011	0.785	1.17±0.04
C2b	6048.	2.063	0.22	4.29	1.31	98.14	2111.	0.091	0.035	0.43	2.0	0.007	0.837	1.20±0.03
C2c	6048.	2.063	0.22	4.29	1.31	98.20	2112.	0.091	0.035	0.43	2.0	0.007	0.837	1.20 ± 0.03
C3	6021.	2.066	0.22	4.28	1.32	98.14	2088.	0.081	0.034	0.31	1.3	0.004	0.807	1.21 ± 0.04
C4	6108.	2.055	0.22	4.28	1.28	98.13	2046.	0.084	0.036	0.32	3.6	0.018	0.819	1.15±0.03
C5 C6	6117.	2.053 2.062	0.22	4.32 4.29	1.28 1.32	103.73 98.45	2244. 2119.	0.083 0.083	0.033 0.034	0.34 0.33	1.0 1.1	0.000	0.798 0.807	1.21 ± 0.04
C0 C7	6024. 6013.	2.052	0.23 0.22	4.29	1.32	98.43 98.27	2119.	0.083	0.034	0.33	1.1	0.003	0.807	1.21±0.03 1.22±0.03
$\frac{C7}{D1}$	6116.	2.053	0.22	4.30	1.28	101.73	2143.	0.075	0.032	0.33	2.0	0.043	0.769	1.18±0.03
D2a	6051.	2.063	0.22	4.28	1.31	98.13	2060.	0.077	0.032	0.33	2.0	0.044	0.782	1.18±0.03
D2b	6050.	2.068	0.22	4.29	1.31	98.14	2093.	0.089	0.034	0.43	2.0	0.036	0.818	1.19 ± 0.03
D2c	6049.	2.065	0.22	4.28	1.31	98.20	2080.	0.084	0.034	0.39	2.0	0.040	0.804	1.19 ± 0.03
D3	6022.	2.066	0.22	4.28	1.32	98.14	2087.	0.086	0.034	0.41	1.6	0.034	0.808	1.20±0.04
D4	6103.	2.056	0.22	4.28	1.29	98.13	2039.	0.084	0.033	0.36	3.2	0.049	0.808	1.15 ± 0.03
D5 D6	6115. 6020.	2.053 2.058	0.22 0.19	4.29 4.29	1.28 1.32	100.74 98.31	2128. 2100.	0.084 0.083	0.033 0.034	0.38 0.39	2.4 1.3	0.040 0.030	0.798 0.800	1.17±0.05 1.21±0.03
D0 D7	6047.	2.038	0.19	4.29	1.32	98.30	2100.	0.085	0.034	0.39	1.5	0.036	0.803	1.21±0.03 1.21±0.03
$\frac{E1}{E1}$	6103.	2.051	0.22	4.27	1.28	99.04	2030.	0.063	0.040	0.00	2.0	0.032	0.756	1.14±0.05
E2a	6036.	2.064	0.22	4.28	1.32	98.13	2073.	0.095	0.035	0.46	2.0	0.007	0.861	1.19±0.03
E2b	6062.	2.061	0.22	4.29	1.30	98.14	2114.	0.096	0.035	0.48	2.0	0.008	0.859	1.19 ± 0.03
E2c	6069.	2.062	0.22	4.29	1.30	98.20	2091.	0.089	0.035	0.38	2.0	0.005	0.839	1.18 ± 0.03
E3	6023.	2.065	0.22	4.28	1.32	98.14	2086.	0.092	0.035	0.44	1.5	0.004	0.850	1.20 ± 0.04
E4 E5	6044.	2.063	0.23	4.29 4.32	1.31	98.17 103.98	2108. 2251.	0.090	0.035	0.41	1.5 0.7	0.004	0.838	1.20 ± 0.03
E3 E6	6116. 6107.	2.053 2.098	0.22 0.28	4.32	1.28 1.30	99.19	2231. 2096.	0.083 0.082	0.033 0.035	0.34 0.32	2.0	0.000	0.799 0.810	1.22±0.04 1.18±0.03
E7	6015.	2.019	0.23	4.29	1.31	98.37	2127.	0.082	0.033	0.32	1.4	0.010	0.839	1.10±0.03 1.20±0.03
F1	6116.	2.053	0.22	4.29	1.28	101.37	2128.	0.075	0.033	0.29	2.0	0.028	0.771	1.17±0.03
F2a	6069.	2.061	0.22	4.28	1.30	98.13	2043.	0.066	0.033	0.23	2.0	0.039	0.751	1.16±0.03
F2b	6054.	2.063	0.22	4.28	1.31	98.14	2067.	0.081	0.034	0.33	2.0	0.024	0.798	1.18 ± 0.03
F2c	6071.	2.084	0.22	4.27	1.31	98.17	2035.	0.069	0.034	0.24	2.0	0.038	0.759	1.17±0.03
F3	6022.	2.065	0.22	4.28	1.32	98.14	2087.	0.097	0.035	0.51	2.0	0.017	0.852	1.20 ± 0.03
F4 F5	6108. 6116.	2.055 2.053	0.22 0.22	4.27 4.32	1.28 1.28	98.13 104.16	2034. 2251.	0.084 0.083	0.035 0.033	0.33 0.38	3.2 1.0	0.033 0.011	0.811 0.786	1.14±0.03 1.22±0.04
F6	6009.	2.061	0.22	4.29	1.33	98.28	2110.	0.083	0.033	0.37	0.9	0.011	0.780	1.22±0.04 1.22±0.03
F7	6085.	2.097	0.21	4.28	1.31	98.29	2061.	0.077	0.034	0.30	2.0	0.027	0.786	1.18±0.03
<i>G</i> 1	6116.	2.053	0.22	4.29	1.28	101.33	2126.	0.073	0.033	0.28	2.0	0.030	0.767	1.17±0.04
G2a	6029.	2.065	0.22	4.28	1.32	98.14	2080.	0.093	0.035	0.46	2.0	0.019	0.838	1.20 ± 0.03
G2b	6049.	2.064	0.22	4.29	1.31	98.14	2113.	0.095	0.035	0.48	2.0	0.018	0.842	1.20±0.03
G2c	6056.	2.063	0.22	4.28	1.31	98.19	2064.	0.080	0.034	0.32	2.0	0.026	0.792	1.18 ± 0.03
<i>G</i> 3 <i>G</i> 4	6022.	2.066 2.055	0.22 0.21	4.28 4.28	1.32 1.28	98.14 98.30	2086. 2046.	0.096 0.084	0.035 0.035	0.49 0.34	2.0 3.2	0.019 0.033	0.849 0.811	1.20±0.03 1.14±0.03
G4 G5	6114. 6116.	2.055	0.21	4.28	1.28	98.30 104.10	2046. 2251.	0.084	0.033	0.34	1.0	0.033	0.811	1.14±0.03 1.22±0.04
G6	6010.	2.073	0.22	4.29	1.33	98.29	2122.	0.083	0.033	0.37	0.8	0.012	0.787	1.22±0.04 1.23±0.03
<i>G</i> 7	6007.	2.080	0.21	4.29	1.33	98.28	2128.	0.085	0.034	0.39	0.7	0.011	0.804	1.23±0.03
<i>H</i> 1	6116.	2.054	0.22	4.29	1.28	101.32	2126.	0.074	0.033	0.28	2.0	0.030	0.769	1.17±0.04
H2a	6035.	2.065	0.22	4.28	1.32	98.13	2075.	0.090	0.035	0.43	2.0	0.019	0.828	1.19±0.03
H2b	6053.	2.062	0.22	4.28	1.31	98.14	2087.	0.087	0.034	0.39	2.0	0.020	0.817	1.19±0.03
H2c	6054.	2.064	0.22	4.28	1.31	98.20	2077.	0.084	0.034	0.36	2.0	0.022	0.807	1.18 ± 0.03
H3 H4	6022. 6109.	2.066 2.054	0.22 0.22	4.28 4.28	1.32 1.28	98.14 98.13	2086. 2036.	0.089 0.084	0.034 0.035	0.41 0.33	1.6 3.2	0.017 0.032	0.820 0.810	1.20±0.03 1.14±0.03
H4 H5	6116.	2.054	0.22	4.28	1.28	98.13 104.17	2036. 2253.	0.084	0.033	0.38	1.0	0.032	0.810	1.14±0.05 1.22±0.05
H6	6014.	2.086	0.22	4.29	1.33	98.38	2125.	0.083	0.033	0.38	0.8	0.011	0.797	1.22 ± 0.03 1.23 ± 0.03
H7	6011.	2.089	0.23	4.29	1.34	98.29	2125.	0.084	0.034	0.39	0.8	0.013	0.800	1.23±0.03
<i>I</i> 1	6116.	2.053	0.22	4.29	1.28	101.29	2127.	0.072	0.021	0.38	2.0	0.088	0.769	1.17±0.03
<i>I</i> 2a	6050.	2.063	0.22	4.28	1.31	98.13	2061.	0.078	0.024	0.42	2.0	0.086	0.796	1.18 ± 0.03

Y. Lebreton and M.J. Goupil: "À la carte" stellar age-dating and weighing with asteroseismology

Table A.5. continued.

Model	$T_{ m eff}$	L	[Fe/H]	$\log g$	R	$\langle \Delta \nu \rangle$	$\nu_{ m max}$	$\langle r_{02} \rangle$	$\langle rr_{01/10} \rangle$	X_C	$\frac{\Delta Y}{\Delta Z}$	$M_{\rm cc}$	$R_{\rm zc}$	$M_{\rm p} \sin i$
	[K]	$[L_{\odot}]$	[dex]	[dex]	$[R_{\odot}]$	$[\mu Hz]$	$[\mu Hz]$	_	_	_	ΔZ.	$[M_{\star}]$	$[R_{\star}]$	$[M_{ m Jupiter}^{ m r}]$
<i>I</i> 2b	6051.	2.063	0.22	4.28	1.31	98.14	2089.	0.087	0.027	0.48	2.0	0.082	0.818	1.19±0.03
I2c	6053.	2.064	0.22	4.28	1.31	98.19	2080.	0.084	0.026	0.46	2.0	0.083	0.810	1.19 ± 0.03
<i>I</i> 3	6022.	2.066	0.22	4.28	1.32	98.14	2087.	0.085	0.027	0.48	1.6	0.078	0.813	1.20 ± 0.04
<i>I</i> 4	6065.	2.062	0.22	4.28	1.30	98.14	2072.	0.083	0.026	0.45	2.3	0.086	0.810	1.18 ± 0.03
<i>I</i> 5	6044.	2.066	0.20	4.34	1.31	106.11	2392.	0.086	0.031	0.49	0.0	0.000	0.775	1.31 ± 0.04
<i>I</i> 6	6041.	2.020	0.22	4.29	1.30	99.37	2119.	0.082	0.026	0.46	1.7	0.078	0.801	1.19 ± 0.03
<i>I</i> 7	6011.	2.090	0.23	4.29	1.34	98.30	2126.	0.083	0.027	0.49	0.8	0.071	0.801	1.23 ± 0.03
<i>J</i> 1	6116.	2.053	0.22	4.30	1.28	101.35	2130.	0.071	0.012	0.42	2.0	0.125	0.769	1.17±0.04
J2a	6031.	2.065	0.22	4.28	1.32	98.13	2078.	0.090	0.024	0.52	2.0	0.121	0.829	1.20 ± 0.03
J2b	6048.	2.061	0.22	4.29	1.31	98.14	2097.	0.089	0.023	0.51	2.0	0.121	0.824	1.19 ± 0.03
J2c	6051.	2.063	0.22	4.28	1.31	98.19	2085.	0.085	0.021	0.49	2.0	0.122	0.812	1.19 ± 0.03
J3	6022.	2.066	0.22	4.28	1.32	98.14	2087.	0.086	0.022	0.51	1.6	0.119	0.815	1.20 ± 0.03
J4	6116.	2.053	0.22	4.28	1.28	98.13	2037.	0.084	0.020	0.44	3.4	0.134	0.817	1.14 ± 0.03
J5	6228.	2.022	0.24	4.42	1.22	120.50	2807.	0.097	0.031	0.70	0.0	0.085	0.760	1.34 ± 0.05
J6	6081.	2.057	0.26	4.30	1.29	100.14	2149.	0.089	0.023	0.51	2.0	0.122	0.813	1.20 ± 0.03
J7	6014.	2.039	0.22	4.29	1.32	98.28	2113.	0.086	0.022	0.51	1.5	0.116	0.811	1.21 ± 0.03
<i>K</i> 1	6116.	2.054	0.22	4.29	1.28	101.54	2124.	0.076	0.034	0.29	2.0	0.021	0.687	1.17±0.04
K2a	6046.	2.063	0.22	4.28	1.31	98.13	2064.	0.086	0.034	0.37	2.0	0.015	0.746	1.18 ± 0.03
<i>K</i> 2b	6051.	2.064	0.22	4.28	1.31	98.14	2085.	0.090	0.035	0.42	2.0	0.014	0.762	1.19 ± 0.03
K2c	6055.	2.062	0.22	4.28	1.31	98.20	2063.	0.082	0.034	0.34	2.0	0.018	0.740	1.18 ± 0.03
<i>K</i> 3	6022.	2.066	0.22	4.28	1.32	98.14	2087.	0.086	0.034	0.39	1.4	0.011	0.744	1.20 ± 0.03
<i>K</i> 4	6109.	2.054	0.22	4.27	1.28	98.13	2025.	0.084	0.035	0.33	3.4	0.027	0.745	1.14 ± 0.03
<i>K</i> 5	6116.	2.053	0.22	4.32	1.28	104.40	2247.	0.083	0.033	0.38	1.0	0.007	0.700	1.22 ± 0.04
<i>K</i> 6	6061.	2.121	0.26	4.29	1.32	98.46	2111.	0.086	0.034	0.40	1.4	0.018	0.745	1.22 ± 0.03
<i>K</i> 7	6011.	2.033	0.26	4.28	1.32	98.31	2089.	0.084	0.034	0.37	1.6	0.017	0.727	1.20 ± 0.03